



High-Content Monitoring of Drug Effects in a 3D Spheroid Model

Frédérique Mittler¹, Patricia Obeïd¹, Anastasia V. Rulina^{1,2}, Vincent Haguët¹, Xavier Gidrol^{1*} and Maxim Y. Balakirev^{1*}

¹ Université Grenoble Alpes, CEA, INSERM, BIG, BGE, Grenoble, France, ² Université Lyon 1, ENS de Lyon, INSERM, CNRS, CIRI, Lyon, France

OPEN ACCESS

Edited by:

Ruggero De Maria,
Università Cattolica del
Sacro Cuore, Italy

Reviewed by:

Gabriele Gamerith,
Innsbruck Medical University, Austria
Micol Eleonora Fiori,
Istituto Superiore di Sanità, Italy

*Correspondence:

Xavier Gidrol
xavier.gidrol@cea.fr;
Maxim Y. Balakirev
maxim.balakirev@cea.fr

Specialty section:

This article was submitted
to Cancer Molecular
Targets and Therapeutics,
a section of the journal
Frontiers in Oncology

Received: 20 June 2017

Accepted: 15 November 2017

Published: 11 December 2017

Citation:

Mittler F, Obeïd P, Rulina AV,
Haguët V, Gidrol X and Balakirev MY
(2017) High-Content Monitoring of
Drug Effects in a 3D Spheroid Model.
Front. Oncol. 7:293.
doi: 10.3389/fonc.2017.00293

A recent decline in the discovery of novel medications challenges the widespread use of 2D monolayer cell assays in the drug discovery process. As a result, the need for more appropriate cellular models of human physiology and disease has renewed the interest in spheroid 3D culture as a pertinent model for drug screening. However, despite technological progress that has significantly simplified spheroid production and analysis, the seeming complexity of the 3D approach has delayed its adoption in many laboratories. The present report demonstrates that the use of a spheroid model may be straightforward and can provide information that is not directly available with a standard 2D approach. We describe a cost-efficient method that allows for the production of an array of uniform spheroids, their staining with vital dyes, real-time monitoring of drug effects, and an ATP-endpoint assay, all in the same 96-well U-bottom plate. To demonstrate the method performance, we analyzed the effect of the preclinical anticancer drug MLN4924 on spheroids formed by VCaP and LNCaP prostate cancer cells. The drug has different outcomes in these cell lines, varying from cell cycle arrest and protective dormancy to senescence and apoptosis. We demonstrate that by using high-content analysis of spheroid arrays, the effect of the drug can be described as a series of EC50 values that clearly dissect the cytostatic and cytotoxic drug actions. The method was further evaluated using four standard cancer chemotherapeutics with different mechanisms of action, and the effect of each drug is described as a unique multi-EC50 diagram. Once fully validated in a wider range of conditions, this method could be particularly valuable for phenotype-based drug discovery.

Keywords: spheroids, 3D model, prostate cancer, MLN4924, HCS screening, drug discovery, ubiquitin, Nedd8

INTRODUCTION

Past decades have witnessed a significant decline in the discovery of novel medications, which challenges the efficacy and even the validity of the modern drug discovery process (1–3). Among the identified causes of this failure is overreliance on the use of reductionist biological models in preclinical drug trials and, specifically, the use of immortalized cell lines cultured in an unnatural 2D setting (1). It is widely accepted that transformed cells growing in a monolayer on plastic dishes have little in common with the complex 3D multicellular organization found in living organisms. Awareness of this discrepancy has led to studies to find more appropriate cellular models to better represent human physiology and disease for drug screening. These models include long-known multicellular spheroids (4, 5) as well as more sophisticated recent developments, such as

organotypic cultures and organoids (6–8), organ-on-a-chip (9, 10), and 3D-printed tissues (11). However, it should be noted that currently, few of these models can be implemented in classical drug discovery processes, which rely on high-throughput screening of thousands of chemical and biological entities in highly standardized assay conditions. Indeed, the increasing complexity of a model inevitably jeopardizes assay robustness, parallelization, integration, and data analysis, which are essential for standardization. It also boosts the cost of initial screening, although it can be worthwhile in subsequent clinical trials.

To date, the best compromise seems to be the use of spheroid-based models (4, 12, 13) because some of them can be easily standardized, and yet, they provide enough complexity to represent certain aspects of human tissues/tumors, such as 3D geometry; physical, chemical, and biological gradients; cell stratification; and functional differentiation. Spheroid culture is as old as cell culture itself (14, 15): the first pioneer that worked with cell cultures previously documented that “groups of cells round themselves off into little spheres” (16). Subsequent milestone works by Moscona in the 1950s (17) and Sutherland in the 1970s (18) led to the development of modern spheroid models as the preferred *in vitro* 3D platform for drug screening (4, 19–23).

Spheroids are formed by aggregation of cells into tight well-defined rounded objects. Many techniques have been developed to generate spheroids (12, 24), including growing cells in spinner flasks (25), in hanging drops (26), in levitation (27), or microgravity (28) within a natural (29, 30) or synthetic (31) polymer matrix and in liquid-overlay culture on agar- (32), agarose- (22), or polyHEMA-coated (33, 34) plates. In particular, agarose coating of standard microtiter plates creates concave-bottomed wells used to produce an array of individual spheroids and subsequent large-scale drug screening in a 3D format (20, 22, 23). However, because of reproducibility issues, in-lab coating is not always suitable for automated spheroid imaging (21).

To address the growing demand for highly standardized multiplex spheroid assays, several companies have developed spheroid-specific consumables, which include hanging-drop plates, ultra-low attachment (ULA) and similar plates, and micro/nanostructured plates and inserts (19). Among them, U-bottomed ULA plates have become the most popular due to the ease of use and compatibility with the majority of screening readouts [Table 1; (19)].

In particular, Corning-spheroid and InSphero GravityTRAP™ ULA plates facilitate the generation of highly uniform spheroids and their high-throughput/content analysis using bright-field and fluorescence microscopy. These plates are optimal for real-time monitoring of drug-induced changes in spheroid phenotypes.

However, it should be noted that ULA consumables remain rather expensive, and their use may not be necessary because similar quality results can be obtained with a simpler approach. Since the introduction of plasticware in cell culture, it has been known that a non-treated polystyrene surface is cell repelling (34–36), and early works from the Sutherland laboratory previously used this property for spheroid generation (37). By examining several commercially available U-bottomed non-treated plates, we found that the Falcon® 96 Non-Treated Assay plate [henceforth “NTA plate,” Table 1] facilitates efficient spheroid assembly with a number of prostate cell lines. Moreover, excellent optical properties make them compatible with colorimetric, fluorescence, and even chemiluminescence assays as well as with various types of readout devices, such as standard and lens-free microscopes, high-content imaging systems, and microplate readers. As we demonstrate here, using these plates, the entire workflow from spheroid assembly, through real-time analysis of drug-induced phenotypic changes, to an ATP-endpoint assay can be performed on the same plate without spheroid transfer. This significantly simplifies the method and increases its performance.

One of the principal promises of the spheroid model in drug screening is that the more natural 3D setting will allow for more efficient identification of cancer-killing drugs or drugs potentially dangerous to normal cells. As a result, the most studied parameter of drug effects is cytotoxicity. Compared with cells in 2D monolayer culture, spheroids have an important advantage: their larger size. Thus, often, drug cytotoxicity can easily be followed over time by measuring the size and shape of spheroids (21, 38, 39). Furthermore, complex processes, such as tumor invasion and angiogenesis, can be modeled using spheroids, and the effect of drugs can be studied with simple bright-field microscopy (21, 40). Alternatively, the effect of drugs on cell composition, localization, and functional status within the spheroid can be analyzed using fluorescence microscopy, i.e., with immunofluorescence staining (41–43), expression of fluorescent

TABLE 1 | Commercial microtiter plates for 3D spheroid assays.

Microplate	References	Format	Bottom ¹	Color ²	Surface	Company
Corning® Ultra-Low Attachment (ULA) ³	3474, 4520, 4515, 3830, 4516, 7007	96, 384	U	c, b	Grafted hydrogel	Corning Life Sciences
CELLSTAR® Cell-Repellent Surface	650970, 651970	96	U/V	c	Grafted cell-repelling polymer	Greiner Bio-One
GravityTRAP™ ULA	ISP-09-001	96, 384	fV	c, b	Non-adhesive coating (NAC)	InSphero
CellCarrier® ULA	6055330, 6055334	96	U	c	NAC	PerkinElmer
Nunc™ Sphera™	174925, 174929	96	U	c	Sphera™ NAC	Thermo Fisher Scientific
PrimeSurface	MS-9096, MS-9384	96, 384	U/V/Sp	c, w	Grafted hydrophilic polymer	Sumitomo Bakelite
Nexcelom3D ULA	ULA-96U, ULA-384U	96, 384	U	c	NAC	Nexcelom Bioscience
Falcon® 96 Non-Treated Assay	353910	96	U	c	Crystal-grade virgin polystyrene	Corning Life Sciences

The microplate used in the present work is highlighted in yellow. (1) fV: wells with a V profile and a flat bottom. Sp: spindle shaped well; (2) c, clear; b, black; w, white; and (3) including Corning®-spheroid plates.

proteins (44–46), and fluorescent probes (45). The latter is the most suited to a generic method for spheroid monitoring because it does not require spheroid fixation and can be applied to various types of cells.

Many fluorescent probes have been used in spheroid studies (Table 2), most often nuclear staining with Hoechst 33342 and viability measurements with Calcein-AM/Ethidium homodimer 1 (LIVE/DEAD assay, Thermo Scientific). Although cytotoxicity assays remain prevalent, several probes have been utilized for cell tracking or to examine cell function, reactive oxygen species (ROS) formation, mitochondrial activity, and important spheroid physiology parameters, such as oxygen gradient (Table 2).

The primary difference between fluorescence staining of spheroids and monolayer culture staining is the reduced and uneven rate of dye transfer within the compact spheroid mass. This creates dye gradients and increases the time required to reach staining equilibrium. Dye uptake depends not only on the dye structure and type of spheroid but also on spheroid health

and integrity. As a result, staining kinetics may be used as a phenotypic parameter to study the effect of drugs on spheroid state (see Results). However, due to dye cytotoxicity (Hoechst 33342), dye metabolism (Calcein-AM, ROS probes), or signal dilution (CellTrackers), in most published reports, the probes were added shortly before the endpoint assay (45).

In our method, we looked for fluorescent probes that can be used in combination with bright-field microscopy for long-term real-time spheroid imaging. For simple and efficient staining, we chose non-toxic CellEvent™ Caspase-3/7 Green and LysoTracker Deep Red probes that showed persistent spheroid fluorescence (>2 weeks) and provided information complementary to that obtained with bright-field microscopy (Table 2).

Apart from fluorescent staining, numerous standard metabolic assays have been applied to measure spheroid viability. Some of them, e.g., MTT tetrazolium reduction (81) and acid phosphatase assay [APH (22, 82)], use colorimetry, while others are based on fluorescence [Resazurin reduction (83, 84)] or chemiluminescence [ATP assay (85)]. It has been argued that gentle non-lytic

TABLE 2 | Fluorescent probes used for real-time spheroid monitoring.

Probe	Localization	Assay type	Ex/Em	Method	Reference
Hoechst 33342	Nucleus/DNA	Nuclei staining	350/461	HD, NAC, SFM, ULA	(20, 23, 47–53)
DRAQ5	Nucleus/DNA	Nuclei staining	647/665	HD, SFM	(54, 55)
SYTO11	Nucleus/DNA	Nuclei staining	508/527	HD, ULA	(52)
Propidium iodide	Nucleus/DNA	Viability/cytotoxicity	538/617	SFM, ULA	(51, 56)
SYTOX Green	Nucleus/DNA	Viability/cytotoxicity	488/523	NAC	(20, 23)
CellTox Green	Nucleus/DNA	Viability/cytotoxicity	485/530	ULA	(53)
Ethidium dimer	Nucleus/DNA	LIVE/DEAD® assay	528/617	HD, NAC, SFM, ULA	(47, 48, 53, 57–60)
Calcein-AM	Cytoplasm	LIVE/DEAD® assay	494/517	HD, NAC, SFM, ULA	(20, 47, 48, 53, 55–61)
DiOC18(3)	Membranes	Viability	484/501	NAC	(62)
Dihydroethidium	Nucleus/DNA	Cytotoxicity/ROS	518/605	HD, ULA	(52)
DCFDA	Whole cell	Cytotoxicity/ROS	495/529	SFM	(51)
MitoSOX Red	Mitochondria	Cytotoxicity/superoxide	510/580	ULA	(53)
MitoTrackers	Mitochondria	Cytotoxicity	Various	HD, NAC, ULA	(48, 49, 51–53, 63–66)
TMRE, TMRM	Mitochondria	Mitochondrial potential	540/580	HD, NAC, ULA	(52, 66)
Image-iT Assay	Mitochondria/other	Cytotoxicity	Various	ULA	(53)
NAD(P)H-Dye1	Mitochondria/other	Hypoxia/metabolism	537/561	NAC	(67)
CellTrackers	Whole cell	Cell labeling/tracking	Various	HD, NAC, SFM, ULA	(25, 50, 57, 59, 61, 65, 68, 69)
Vybrant DiD	Whole cell	Cell labeling/tracking	644/665	NAC	(20, 70)
Chlorobimane	Whole cell	Cytotoxicity/GSH	394/490	HD, ULA	(52)
ProSense® 680	Whole cell	Proteolysis	680/700	ULA	(71)
Fluo-4-AM	Cytoplasm-Ca ²⁺	Intracellular Ca ²⁺	494/506	ULA	(52, 58)
HypoxiSense 680	Whole cell	Hypoxia/O ₂ gradient	680/700	ULA	(71)
Cyto-ID® HRDR	Whole cell	Hypoxia/O ₂ gradient	596/670	HD, ULA	(72, 73)
NP SII-0.2+	Lysosome/other	Hypoxia/O ₂ gradient	620/760	NAC	(66)
NP NanO2	Cytoplasm	Hypoxia/O ₂ gradient	405/635	NAC	(66)
LOX-1	Whole cell	Hypoxia/O ₂ gradient	488/615	MSS, SFM	(60, 74, 75)
Ru-dpp	Whole cell	Hypoxia/O ₂ gradient	455/613	NAC	(62)
BCECF	Cytoplasm	pH gradient	490/535	NAC	(62)
NP T-probe	Cytoplasm	Temperature gradient	560/578	NAC	(66)
CaspGLOW Red	Cytoplasm	Apoptosis/caspases	540/570	NAC	(62)
Nucview 488	Nucleus/DNA	Apoptosis/caspases	504/534	HD	(76)
CellEvent	Nucleus/DNA	Apoptosis/caspases	511/533	NAC, NTA, ULA	(23, 47, 48, 77)
LysoTrackers	Lysosome/other	Cytotoxicity/apoptosis	Various	NAC, MSS, SFM	(66, 78–80)

The probes used in the present work are highlighted in yellow.

HD, hanging drop; NAC, non-adhesive coating; NTA, non-treated assay; MSS, microstructured surface; SFM, spheroid forming medium/matrix; ULA, ultra-low attachment; ROS, reactive oxygen species.

assays, such as MTT or Resazurin reduction assays, may not be efficient with spheroids because of the incomplete probe penetration (86). In addition, a colorimetric APH assay has a limited sensitivity and requires spheroid transfer (22). Today, the most robust metabolic endpoint assay seems to be the measurement of spheroid ATP content *via* chemiluminescence. Efficient ATP extraction is achieved by harshening (compared with monolayer culture) the lysis conditions or by using commercial 3D-specific reagents (38, 85). The chemiluminescence method has excellent sensitivity, and as we demonstrate in the present report, the ATP content of a single spheroid can be quantified reliably in the same U-bottomed plate after completion of phenotypic analysis.

To demonstrate the method performance, we analyzed the effect of the preclinical anticancer drug MLN4924 (henceforth “MLN”) on spheroids formed by VCaP and LNCaP prostate cancer cells. MLN, an inhibitor of Nedd8-activating enzyme (NAE), blocks intracellular proteolysis mediated by cullin-RING E3 ligases (87). MLN is currently being evaluated in clinical trials for the treatment of hematologic malignancies and solid tumors (88, 89). Different cancer cells have different sensitivities to MLN, and as we have shown recently (77), MLN treatment has complex outcomes that vary from cell cycle arrest and protective dormancy to senescence and apoptosis. Here, we show that the complexity of the effects of MLN as well as of other cancer therapeutics with different mechanisms of action (MOAs) can be addressed using the 3D spheroid method.

MATERIALS AND METHODS

Materials

Falcon® 96 Well Clear Round Bottom Non-Treated Assay plates (NTA plates, Corning #353910) and White 96 Well Transparent Bottom CELLSTAR® plates (white plates, Greiner Bio-One #655088) were purchased from Dominique Dutscher (Grenoble, France). Universal polystyrene lids (Thermo Fisher Scientific #5500), Dulbecco's modified Eagle's medium (DMEM, Gibco #41966), Roswell Park Memorial Institute medium (RPMI1640, Gibco #61870), Keratinocyte Serum Free Medium (K-SFM) kit supplied with bovine pituitary extract (BPE), and human epidermal growth factor (EGF) (Gibco #17005-042), Dulbecco's phosphate-buffered saline (PBS) without calcium or magnesium (Gibco #14190), 0.05% trypsin-EDTA (Gibco #25300054), 10 kU/mL penicillin-streptomycin (Gibco #15140122), CellEvent Caspase-3/7 Green Reagent (Invitrogen #C10423), and LysoTracker Deep Red (Invitrogen #L12492) were obtained from Thermo Fisher Scientific (Courtaboeuf, France). Fetal bovine serum (FBS, PAN Biotech #P30-3302) was purchased from Dominique Dutscher (Grenoble, France). ViaLight™ Plus Cell Proliferation and Cytotoxicity BioAssay Kit (Lonza #LT07-121) were obtained from Lonza (Basel, Switzerland). For chemotherapy drugs, MLN4924 (MLN, MedChemExpress #LSG790) was purchased from Interchim (Montluçon, France), cisplatin (Cayman Chemical #CAYM13119-250) from VWR International (Fontenay-sous-Bois, France), docetaxel (Acros Organics, #15316097) from Thermo Fisher Scientific, Etoposide (Aldrich, #E1383) from Sigma-Aldrich (Saint-Quentin-Fallavier,

France), and ARN-509 (Adooq Bioscience, #A11923-10) from CliniSciences (Nanterre, France).

Cell Lines

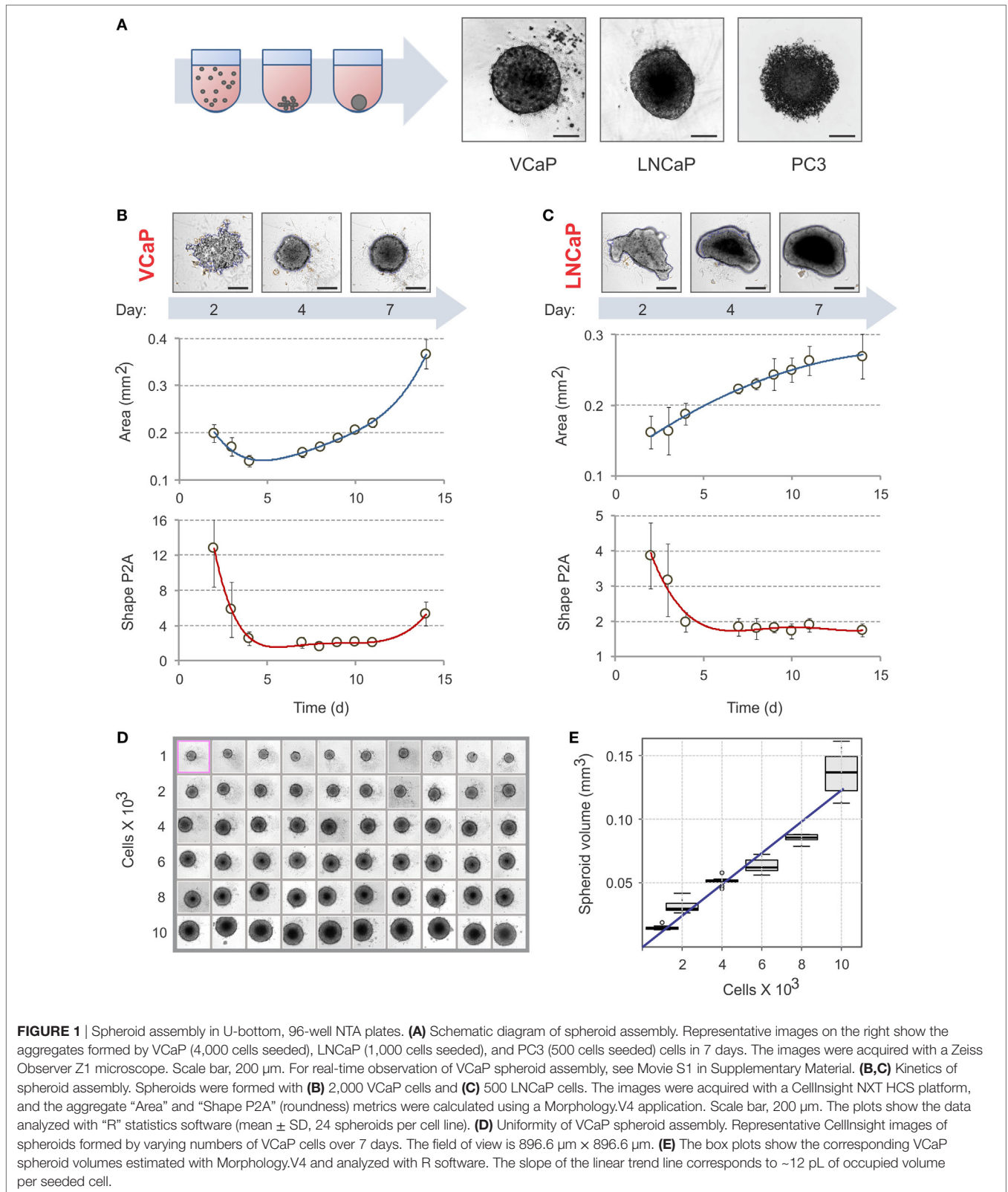
The VCaP (androgen receptor-positive, androgen-sensitive, containing *TMPRSS-ERG* translocation, p53-R248W, PTEN-wt; ATCC #CRL-2876), LNCaP (androgen receptor-positive, androgen dependent, p53-wt, PTEN-mut; ATCC #1740), PC3 (androgen receptor-negative, androgen independent, p53-null, PTEN-null; ATCC #CRL-1435), DU145 (androgen receptor-negative, androgen-independent, p53-P223L-V274F, PTEN-wt; ATCC #HTB-81), and RWPE-1 (HPV18-immortalized normal adult prostate epithelial cells; ATCC #CRL-11609) cell lines were purchased from American Type Culture Collection (ATCC). The DuCaP cell line (similar origin as VCaP) was kindly provided by Prof. Jack Schalken from the Radboud University Nijmegen Medical Center, who originally received them from Kenneth J. Pienta, MD, Director of Research at The Brady Urological Institute, Baltimore, where this cell line was created (90). The PNT2 cell line (SV40-immortalized normal adult prostate epithelial cells; ECACC #95012613-1VL) was purchased from the European Collection of Authenticated Cell Cultures (ECACC).

Cell lines were tested on a semester basis for AR, PSA, SLC45A3, and ERG using quantitative RT-PCR. VCaP and DU145 cells were cultured in DMEM containing 10% FBS and 1% penicillin-streptomycin (complete growth medium). LNCaP, PC3, DuCaP, and PNT2 cells were cultured in RPMI1640 with the same supplements. RWPE-1 cells were cultured in K-SFM containing 0.05 mg/mL BPE, 5 ng/mL EGF, and 1% penicillin-streptomycin. The cells were grown in an incubator at 37°C, 5% CO₂, and 95% humidity. For different passages, the cells were washed twice with PBS followed by the addition of trypsin-EDTA and incubation for 3–10 min depending on the cell line. Subculture was performed depending on the density of the cells. Typically, for VCaP cells, subculture was performed once per week, at 1/2 dilution; LNCaP cells were divided twice per week, at 1/5 dilution.

Spheroid Assembly

Cells were grown in appropriate complete growth medium for at least 3 days in standard T75 flasks to reach approximately 70% confluence. For reproducible results, cells of a similar passage number ($1 < N < 15$) were always used. To prepare the cell suspension, a cell monolayer was washed with 10 mL of PBS and treated with 1.5 mL of a trypsin-EDTA solution for 5 min at 37°C. Trypsin was then neutralized with 8 mL of complete growth medium, and the cell suspension was centrifuged at $400 \times g$ for 5 min. After supernatant removal, the cell pellet was resuspended in 1–3 mL of complete growth medium, and the cell density was determined using a Scepter™ Cell Counter (Merck Millipore). Note that it is critical to ensure that the cell suspension is homogeneous (single cells) and does not contain aggregates, because this determines the size and uniformity of spheroids. The optimal cell density must be determined in preliminary spheroid generation tests (see **Figure 1C**, for example).

The suspension was then diluted with complete growth medium to obtain the final density and dispensed (200 μ l/well) into 96-well NTA plates. To reduce the effect of uneven



evaporation on spheroid formation, the edge wells of the plates were not used and filled with PBS. This resulted in $6 \times 10 = 60$ wells per plate to analyze. The plates were covered with the

universal polystyrene lids and kept in an incubator (37°C, 5% CO₂, 95% humidity) for at least 2 days before imaging. During this period, it is important not to disturb the plates as this can

displace spheroids from the center of the well. In addition, although previous reports (70, 83, 91) have shown that mild centrifugation can promote single spheroid assembly, no significant effect of centrifugation was observed with VCaP and LNCaP cells.

Finally, the analysis of spheroid assembly was conducted immediately after the cell suspension addition when performed on a video microscope (Zeiss Axiovert 200 M) equipped with a cell culture chamber or on a lens-free microscope [VideoCell (92)] within the cell culture incubator.

Analysis of Spheroid Assembly

After 2 days of spheroid formation, the plates were scanned once a day on a CellInsight NXT High Content Screening Platform (Thermo Scientific) equipped with a 10× objective. The acquisition parameters were set using the instrument software HCS Studio 6.5.0. The bright-field channel was used for autofocusing, and the exposure time was set within the 25–35% saturation range according to the HCS Studio recommendations. Acquisition of “one field of view per well” was sufficient for the majority of spheroid measurements and significantly reduced the time required for plate analysis. Using 4 × 4 binning, an 896.6 μm × 896.6 μm field of view was converted into a 552 px × 552 px image. With these settings, the scan of a 96-well plate took approximately 5 min. The images were saved automatically and could be analyzed later.

Image analysis was performed with the instrument software HCS Studio 6.5.0—Morphology.V4. Up to 20 different “Cell-selected features” were chosen for Channel 1. Then, the bright-field images were imported as “Channel 1-Object.” This generated the object masks for each image. The masks were further adjusted by imposing the size range for the counted objects (“Object selection” > 1,000 px² for VCaP, and >3,000 px² for LNCaP) and “Cell-selected features” were calculated for each of the adjusted masks. The object “Area” and “Shape P2A” were the most informative morphometric parameters (see Results). Shape P2A = (Perimeter)²/4π × (Area) represents the object roundness and is equal to 1 for a perfect circle; for less spherical objects, P2A becomes larger than 1. Note that, apart from these features, other calculated parameters, such as object “CircDiameter,” “Sphere Volume,” and “Aspect ratio LWR” were also useful for evaluating spheroid morphology. Next, a table of all calculated features was generated as a .csv file using the “Cellomics-View” application. The data were imported into “R” statistical software to create a fully annotated .csv data file by fusing with the “Experimental Design” table. The mean, median, SD, and quartile values were calculated with “R” software.

For manual acquisition, the images from each well were recorded using an inverted microscope (Zeiss Observer Z1). A 10× objective was primarily used, switching to a 5× objective when an object area was too large. The entire acquisition took approximately 30 min for a 96-well plate. To analyze the images taken on standard and video microscopes, an in-lab ImageJ macro was used. Alternatively, open-source tools, e.g., based on MATLAB (39), ImageJ (83), or Fiji (93), could also be utilized to produce object masks and calculate object area and perimeter.

Spheroid Treatment with MLN4924

The spheroids were formed following the protocol described earlier by incubating 2,000 cells for 7 days (VCaP) or 500 cells for 4 days (LNCaP) in NTA plates. Three replicate plates were prepared per experiment. MLN solutions were prepared immediately before use by diluting 2 mM DMSO stock solution in complete growth medium to a 2× final concentration. The drug solution of the highest concentration was made first and used to prepare all drug dilutions of the series. To avoid the effect of DMSO on spheroid growth, it is critical to ensure that the highest DMSO concentration in spheroid medium does not exceed 0.5%, which corresponds to 1% in drug solutions. Using “6 × 10 wells per plate” and “six spheroids per condition” experimental formats, nine drug concentrations and the DMSO vehicle control could be tested with one NTA plate. This corresponded to 600 μL total volume per plate for each drug dilution.

For apoptosis analysis, CellEvent was added to each of the prepared drug solutions to obtain a 2 μM concentration. Then, 100 μL of spheroid medium was carefully removed from each well (trying not to displace the spheroids from the center of the well) and replaced with 100 μL of CellEvent-drug solution. The plates were kept in an incubator (37°C, 5% CO₂, 95% humidity), and image acquisition was performed once a day.

For viability measurements, a 0.4 μM solution of LysoTracker Deep Red dye was prepared just before use by diluting 1 mM DMSO stock solution in complete growth medium. Then, 10 μL of this solution was added to each well, and imaging was performed at time points defined in the “Experimental Design” table.

Monitoring MLN Effect

The effect of MLN on spheroids was followed using a CellInsight NXT High Content Screening Platform as described earlier. The acquisition parameters were as follows: bright field for Channel 1, CellEvent fluorescence (FITC filter set used) for Channel 2, and LysoTracker Deep Red fluorescence (Cy5 filter set used) for Channel 3. Autofocus was performed in bright field (Channel 1), and the plates were scanned using “one field of view per well” acquisition with 4 × 4 binning. With these settings, the scan of a 96-well plate usually took less than 7 min.

The image analysis was performed using HCS Studio 6.5.0—Morphology.V4 software as described earlier. Up to 30 different “Cell-selected features” were measured for Channels 1–3. The bright-field images were imported as “Channel 1—Object,” CellEvent images as “Channel 2—Member,” and LysoTracker Deep Red images as “Channel 3—Spot/Fiber.” The corresponding masks were generated for each image, and “Cell-selected features” were calculated for each mask. The preferred parameters used for fluorescence analysis of the drug effects were fluorescence “Area,” “Total Intensity,” and “Average Intensity.” The data were analyzed using “R” software.

For manual acquisition, the images were recorded on the inverted microscope with a 10× (5×) objective using bright field, FITC, and Cy5 channels. The analysis was performed using an in-lab ImageJ macro.

ATP-Based Endpoint Assay

Spheroid viability was analyzed by measuring ATP with a ViaLight™ Plus Cell Proliferation and Cytotoxicity BioAssay Kit (Lonza). The manufacturer's protocol was applied with some modifications. Thus, 100 μ L of spheroid medium was carefully removed from each spheroid-containing well of the NTA plate, and 50 μ L of cell lysis reagent was added. The plate was agitated on an orbital shaker for 20 min at room temperature. Note that this protocol has been optimized for VCaP and LNCaP spheroids. For other cell types, the optimal lysis time must be determined in preliminary tests by measuring the efficiency of ATP extraction (using chemiluminescence).

Then, 100 μ L of room-temperature ATP monitoring reagent plus (AMR plus) was added to each well, and the plate was incubated for 2 min at room temperature. Blank solution was prepared by adding cell lysis reagent and AMR plus to complete growth medium. Luminescence was measured on a GloMax®-Multi Detection System (Promega) with a 1 s integration time. Optionally and when higher sensitivity is required, the samples can be transferred into a white plate with a flat transparent bottom (Grenier Bio-One) and remeasured. This may result in an up to threefold increase in signal intensity.

Cell viability in monolayer cultures was measured according to the manufacturer's protocol.

Monitoring the Effect of Chemotherapy Drugs

The effect of chemotherapy drugs (cisplatin, docetaxel, etoposide, and ARN-509) on VCaP and LNCaP spheroids was examined following the protocol described earlier for MLN. Drug stock solutions were prepared in DMSO, with the exception of cisplatin, for which DMF was used (94). Drug dilutions used to generate dose–response curves are given in Table S1 in Supplementary Material.

RESULTS

Spheroid Assembly

Because cell attachment is inhibited in NTA plates, the cells clump together and form 3D spheroids. The U-profile of the wells ensures that only one spheroid per well is formed (**Figure 1A**; Movie S1 in Supplementary Material). As with ULA plates (21), not all cells form spheroids under these conditions. For instance, VCaP and LNCaP prostate cancer cell lines form spheroids while PC3 cells produce only loose aggregates [**Figure 1A**; see also Ref. (21, 33, 95)]. In some cases, modification of the cell culture medium composition could promote spheroid formation in NTA plates. Thus, among the seven prostate cancer cell lines examined in the present work, the majority produced individual spheroids after brief optimization of the culture conditions (Figure S1 in Supplementary Material). Two cell lines, DU145 and PNT2, formed multiple non-uniform spheroid-like aggregates (Figure S1 in Supplementary Material). Because VCaP and LNCaP cells reproducibly form spheroids and have different sensitivities to MLN in monolayer culture (77), we focused our study on these cell lines.

To avoid drug interference with spheroid assembly, spheroids must be well formed before drug treatment. The criteria used in the literature are rather visual and arbitrary (21, 31). We therefore decided to define a measurable parameter of spheroid assembly. Spheroid formation was followed over time with a CellInsight NXT HCS platform and analyzed with the instrument software (**Figures 1B,C**). We found that “Area” and “Shape P2A” are the best direct morphometric parameters to characterize spheroid assembly and growth. For slow-proliferating (in 2D) cells, such as VCaP cells, the minimum of the “Area” curve may represent a characteristic time of spheroid assembly (**Figure 1B**). However, for the faster growing LNCaP cells, the “Area” occupied by the aggregate steadily increased (**Figure 1C**). The best parameter for both cell lines appeared to be “Shape P2A”: when it attains the minimum, the aggregates are considered round and spheroid (**Figures 1B,C**). Using this parameter, a period of 4–7 days was found to be optimal for spheroid assembly. It should be noted that when measuring spheroid assembly, particular attention must be paid to the composition of the culture medium. Thus, we found that small changes in medium FBS, e.g., different concentrations, suppliers, and even lots, may significantly influence spheroid assembly. In addition, charcoal stripping of the serum reduced the rate of spheroid formation by both VCaP and LNCaP cells (Figure S1 in Supplementary Material). Therefore, it seems that spheroid assembly in NTA plates is, at least partially, an active cellular process that depends on specific cues within the culture medium.

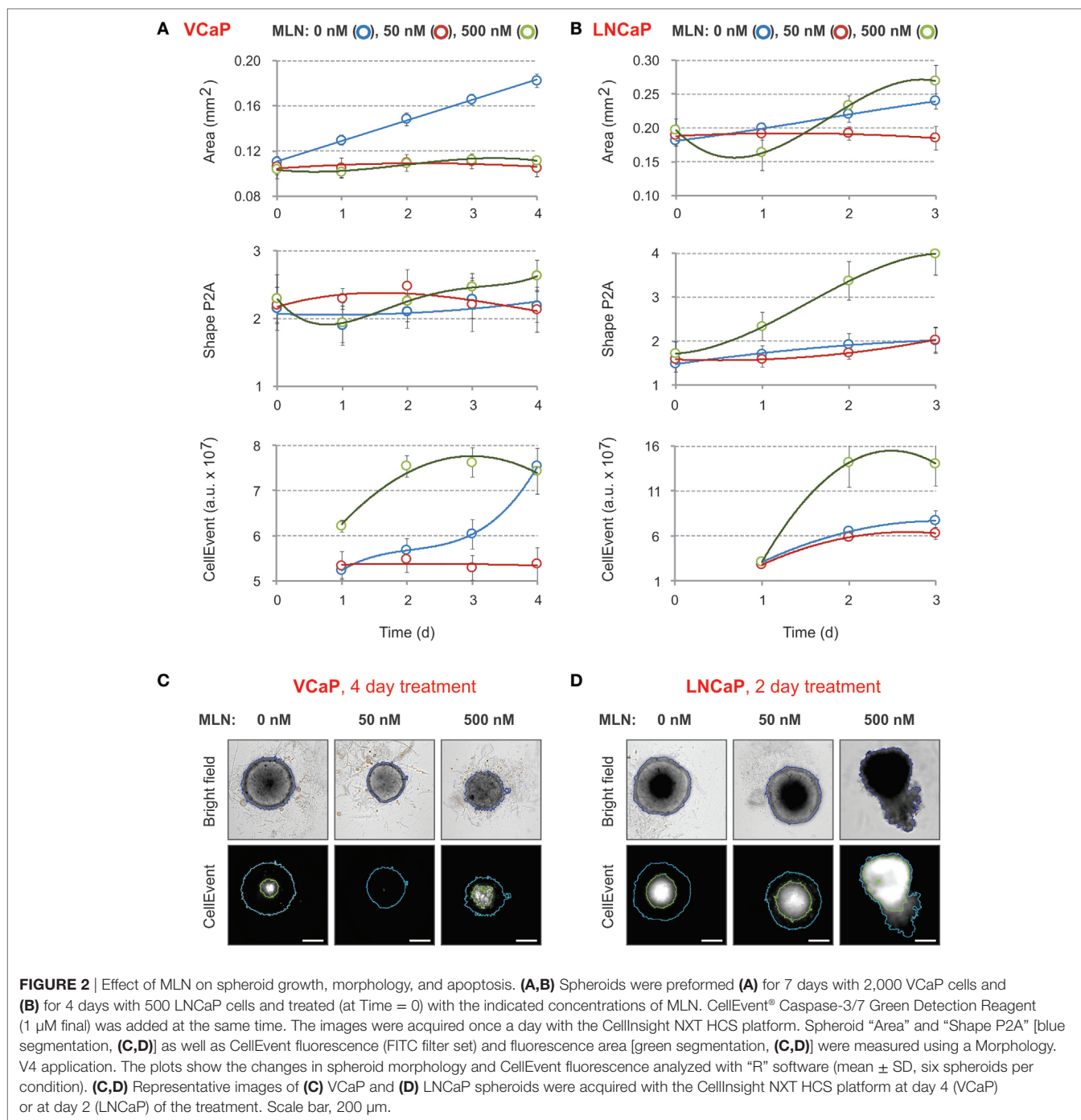
The NTA plates ensured the formation of highly uniform spheroids (**Figure 1D**). Increasing the density of cell seeding resulted in a linear increase in spheroid volume. For VCaP cells, the slope of the trendline corresponded to approximately 12 pL of occupied volume per seeded cell (**Figure 1E**), which fell within the range of 5–20 pL/cell estimated for other spheroids described in the literature (21, 47, 83). This significantly exceeds the size of a VCaP cell (1.3 pL) measured with a Scepter™ Cell Counter, suggesting that cells undergo multiplication upon spheroid assembly. This could also indicate the presence of some extracellular space within the spheroids.

The optimal conditions required to form spheroids of approximately 400 μ m in diameter (21, 31, 83) were determined to be 2,000 cells/well for 7 days with VCaP cells. Because the fast-growing LNCaP spheroids rapidly developed a hypoxic core that interfered with phenotypic measurements (see below), 500 cells/well and a duration of 4 days were used to form LNCaP spheroids.

Effect of MLN on Spheroid Growth, Morphology, and Apoptosis

Having established the optimal conditions for spheroid assembly, we examined the effect of MLN on preformed VCaP and LNCaP spheroids. Of note, in monolayer culture, these cell lines display a marked difference in MLN sensitivity: IC₅₀ of 500 and 50 nM for VCaP and LNCaP cells, respectively.

First, the time course of changes in spheroid size and shape induced by 50 and 500 nM of MLN was analyzed (**Figures 2A,B**). For VCaP cells, at both concentrations, the drug arrested the



growth of spheroids without affecting their roundness (**Figure 2A**, “Area” vs “Shape P2A”). By contrast, automated analysis of LNCaP spheroid growth was not conclusive (**Figure 2B**, “Area”). Visual examination revealed that at 500 nM the drug caused physical disruption of LNCaP spheroids, resulting in an unexpected increase in apparent spheroid size (**Figure 2D**, “Bright field”). The disruption starts on the second day of MLN treatment and is easily detected automatically by measuring spheroid roundness (**Figure 2B**, “Shape P2A”).

These results demonstrate that within the given time-frame simple bright-field analysis of spheroid morphology is not sufficient to characterize the effect of MLN. Indeed, it does not distinguish between two very different drug concentrations in the case of VCaP spheroids, whereas in LNCaP spheroids, it does not reliably detect the toxic effect of 50 nM MLN that corresponds to the IC50 value in monolayer culture. More prolonged drug treatment can partially help but requires reevaluation of culture conditions to prevent spheroid overgrowth.

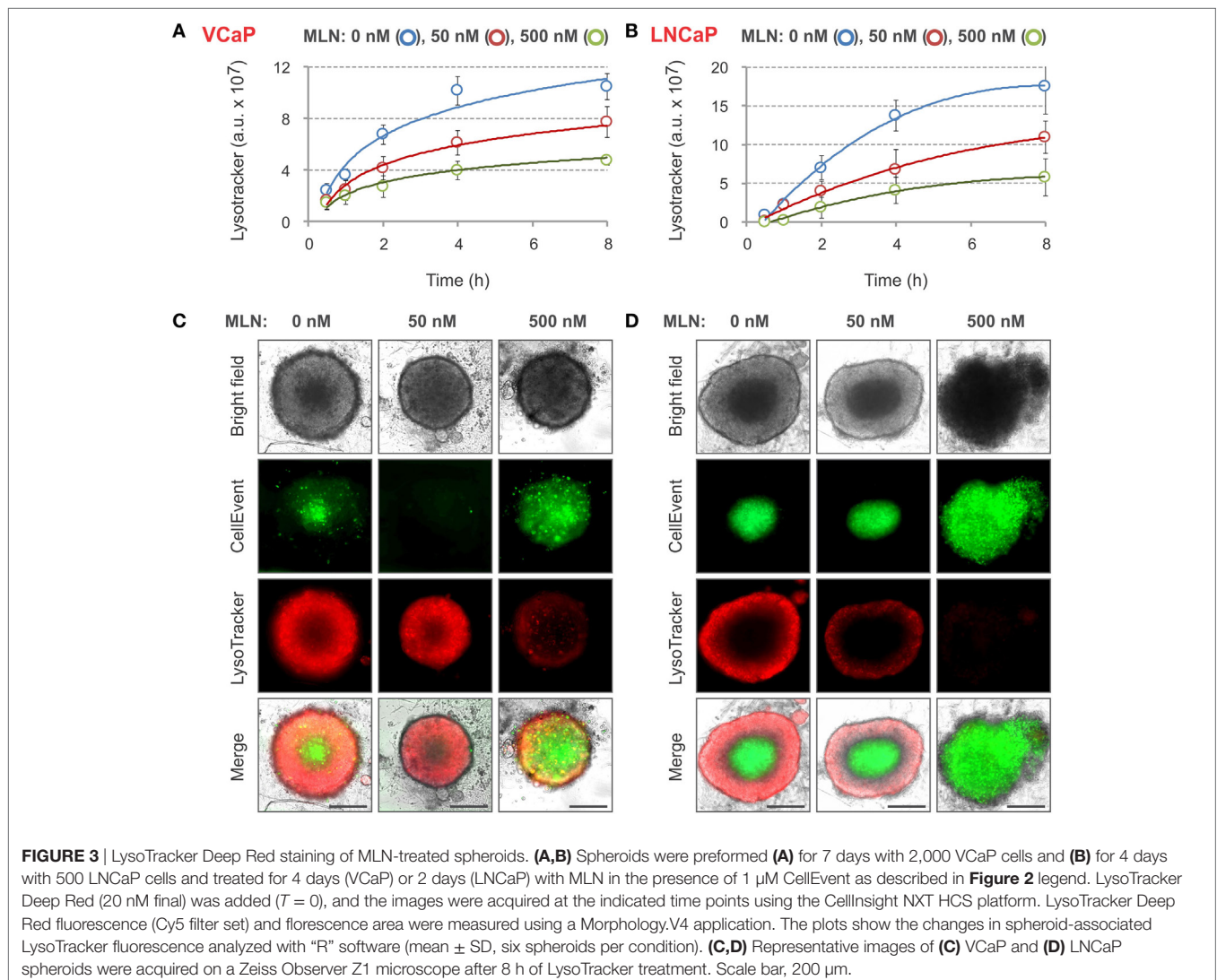
Because MLN induces apoptosis in prostate cancer cells (77), we measured the kinetics of apoptosis induction using CellEvent, a fluorogenic caspase-3/7 substrate (23, 77) (Figures 2C,D, “CellEvent”). The reagent was added to spheroids at the same time as MLN. Drug-induced apoptosis was readily detected in both VCaP and LNCaP spheroids starting from the second day of spheroid treatment with 500 nM MLN (Figures 2A,B, “CellEvent”). In addition, independently of the treatment, all spheroids larger than approximately 450 μm in diameter showed a CellEvent-positive central region consistent with apoptosis induction within the nutrient deprived spheroid core (23, 62, 77). When this signal is so strong that it interferes with the drug cytotoxicity assay, as in LNCaP spheroids (Figure 2D), the measurement of the “fluorescence area” and normalization of the CellEvent signal to the spheroid area may help to distinguish the drug-specific effect. Thus, although the measurement of CellEvent “total intensity” did not distinguish between control and 50 nM MLN conditions (Figure 2B, “CellEvent”), some increase in “fluorescence area” was observed upon drug treatment (Figure 2D). Finally, and consistent with our previous

observation (77), VCaP spheroids growth arrested with 50 nM MLN showed negligible apoptosis, even compared with control conditions (Figure 2C, “CellEvent”).

Compared with the morphometric parameters, the use of CellEvent provides complementary information regarding how the drug induces apoptosis within spheroids. Notably, for all tested concentrations (<2 μM), CellEvent was non-toxic to prostate cancer spheroids (did not change morphometric parameters or ATP content) and ensured a measurable and informative signal for more than 2 weeks of spheroid culture.

Spheroid Staining with LysoTracker Deep Red

Because CellEvent analysis of apoptosis did not detect any significant effect of 50 nM MLN on LNCaP spheroids, we looked for other vital probes that were more sensitive. We found that spheroid staining with LysoTracker Deep Red was inversely proportional to MLN concentration. When added to the spheroids, the fluorescence of LysoTracker steadily increased and then started to plateau after 8 h of incubation (Figures 3A,B). The plateau level



in MLN-pretreated spheroids was maximal in control conditions and decreased with increasing MLN concentration. The staining pattern was complementary to that of CellEvent, with the LysoTracker accumulating in the outer and presumably metabolically active layers of spheroids (Figures 3C,D). This result was unexpected because LysoTrackers are considered to be markers of cytotoxicity, cell senescence and apoptosis (78–80) (Table 2). One possible explanation for this discrepancy is that LysoTracker Deep Red belongs to a different chemical class than LysoTracker Red DND-99, which was used in previous studies (78–80).

Nevertheless, the use of LysoTracker Deep Red allowed for fair quantification of the effect of different doses of MLN with both VCaP and LNCaP spheroids. Similar to CellEvent, LysoTracker Deep Red dye is non-toxic (at tested concentrations <50 nM) and can be used for long-term monitoring of the drug effect in a 3D spheroid model.

Phenotypic Changes Induced by MLN in Prostate Cancer Spheroids

The four parameters described earlier, “Area,” “Shape P2A,” “CellEvent,” and “LysoTracker Deep Red,” allowed for high-content monitoring of the drug effect in real-time. This is an important advantage compared with standard endpoint assays, because it reveals dynamic aspects of drug action and provides a flexible choice to measure dose–response curves. Using this approach, the complexity of the MLN effect, which is not obvious in monolayer culture (77), becomes readily dissected (Figures 4A,B). Thus, in VCaP spheroids, the two major outcomes of MLN treatment were (i) spheroid growth arrest with $EC_{50} = 18$ nM (Figure 4A, “Area”) and (ii) a cytotoxic effect with $EC_{50} > 500$ nM seen by an increase in apoptosis (Figure 4A, “CellEvent”) and a decrease in LysoTracker Deep Red uptake (Figure 4A, “LysoTracker”). A slight decline in total LysoTracker fluorescence at MLN concentration <100 nM most likely reflected the decrease in spheroid size. The quiescent state, characterized by cell cycle arrest and apoptosis inhibition, is easily detected between 25 and 100 nM MLN (Figure 4A). As we previously showed (77), this state is reversible, and removal of the drug results in spheroid regrowth at a normal pace. In the more MLN-sensitive LNCaP spheroids, these two effects could not be separated because of the earlier onset of cytotoxicity manifested by an increase in “CellEvent” ($EC_{50} = 180$ nM, Figure 4B) and a decrease in LysoTracker fluorescence ($EC_{50} = 70$ nM, Figure 4B). The major outcome of MLN treatment of LNCaP spheroids was spheroid disruption (Figure 4B, “Area”: $EC_{50_2} = 190$ nM, and “Shape P2A”: $EC_{50} = 250$ nM). The growth arrest induced by low <100 nM concentrations of MLN was also detected (Figure 4B, “Area”: $EC_{50_1} = 18$ nM), although it was much less defined than in VCaP spheroids.

Viability Measurement with an ATP-Based Endpoint Assay

The phenotypic analysis was complemented by evaluation of spheroid metabolic status using an ATP-based endpoint assay. Usually, this requires spheroid lysis and transfer of the lysate into an opaque-walled flat-bottom plate to measure chemiluminescence.

We found that analysis can be performed in the same U-bottom NTA plate. Although this causes an approximate threefold decrease in signal intensity, the high sensitivity and dynamic range of the method ensure very similar robust results independently of the plate (Figures 5A,B). The ATP response curves most closely matched those measured with LysoTracker Deep Red, with the biphasicity of the VCaP response becoming even more obvious (Figure 5A). Biphasic drug dose–response curves have been documented previously and are attributed to the heterogeneity of cell populations within spheroids (83). However, phenotypic analysis of the MLN effect in VCaP spheroids and the results of our previous work (77) suggest the complexity of the drug action mechanism is the prime cause. Notably, ATP measurements in VCaP monolayer culture did not show a biphasic response to MLN (Figure 5A), and additional assays were required to detect the difference in drug effect at low and high concentrations (77). Alternatively, for LNCaP cells, similar MLN dose–response curves were obtained with either spheroids or monolayer culture (Figure 5B).

Collectively, these results show that high-content spheroid monitoring provides information that goes beyond a simple cytotoxicity assay. Thus, despite a unique target [NAE, with an IC_{50} of approximately 5 nM (87)], inhibition of neddylation by MLN affects multiple cellular processes with different effects on cell viability (77). This explains why MLN toxicity in various cell lines varies significantly. LNCaP cells are 10 times more sensitive than VCaP cells, despite a similar efficiency of neddylation inhibition ($EC_{50} = 8$ –10 nM, Table 3). Some of these effects can be addressed by high-content monitoring. Our analysis shows that spheroid growth is the most sensitive process affected by MLN ($EC_{50} = 18$ nM, Table 3). Because the proposed mechanism of MLN toxicity is proliferation dependent (96), it seems plausible that in VCaP spheroids inhibition of cell proliferation results in protective quiescence [Figure 4A, and Ref (77)], while in the faster-proliferating LNCaP cells, this inhibition is not efficient and does not prevent the onset of apoptosis and cytotoxicity (Figure 4B).

Monitoring the Effect of Chemotherapy Drugs

To further evaluate the method, the effect of four anticancer drugs used for prostate cancer chemotherapy was examined. The following compounds with distinct MOAs were chosen: docetaxel, a microtubule-binding anti-mitotic agent, which is the most commonly used “standard of care” drug for castration-resistant prostate cancer (CRPC) (97, 98); cisplatin, a DNA-crosslinking chemotherapeutic agent, and etoposide, a topoisomerase II inhibitor, which are evaluated in combination therapies for some resistant CRPC phenotypes (98, 99); and ARN-509, a novel antiandrogen for prostate cancer treatment (100), which was recently submitted to the FDA for approval.

The experimental conditions established in the MLN study were used. Four parameters, “Area,” “Shape P2A,” “CellEvent,” and “LysoTracker Deep Red,” were measured to build dose–response curves with VCaP and LNCaP spheroids (Figures S2–S5 in Supplementary Material). At the end of the treatments (2 days

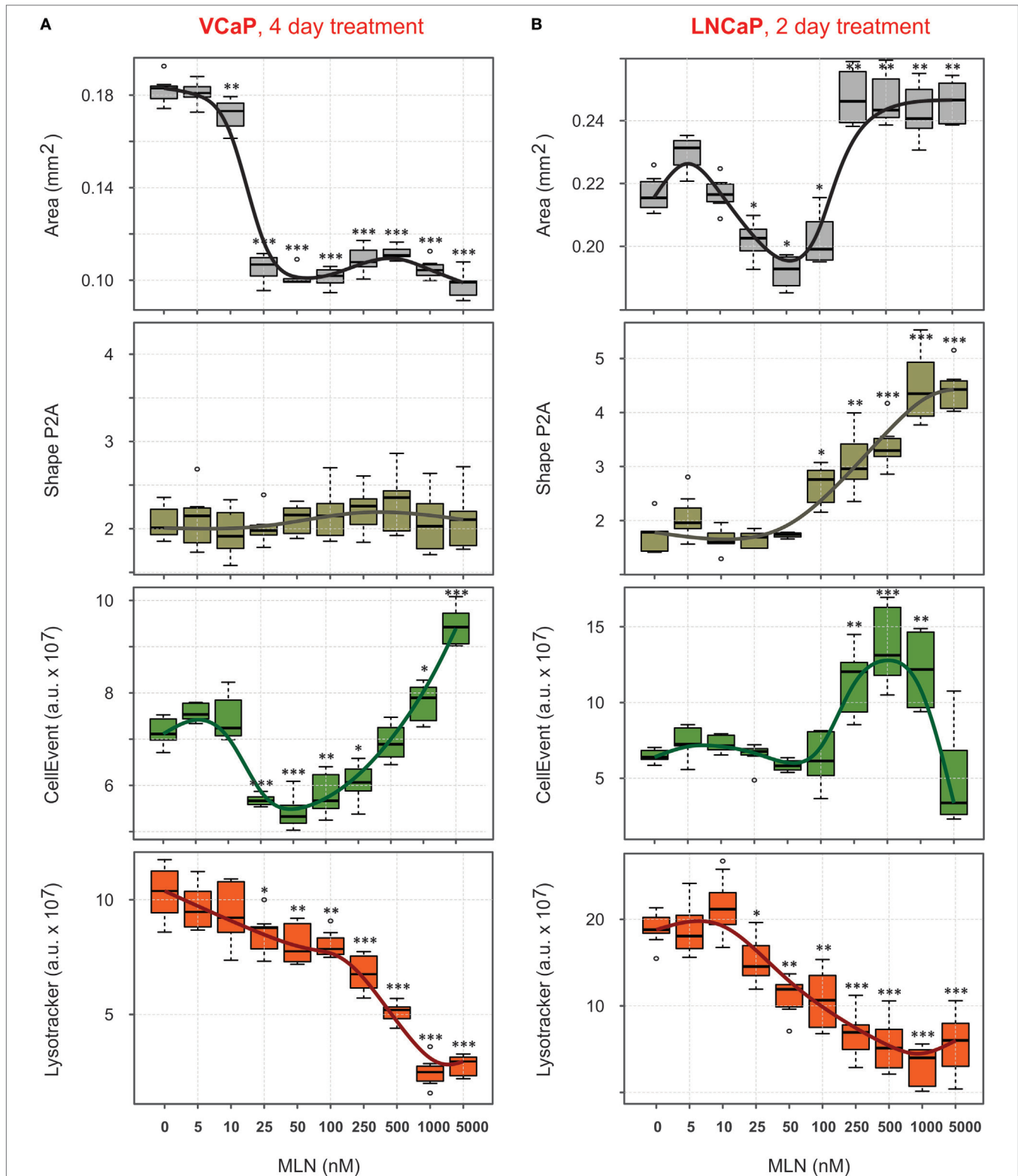


FIGURE 4 | Quantification of phenotypic changes induced by MLN in prostate cancer spheroids. **(A,B)** Preformed spheroids were treated for 4 days [VCaP, **(A)**] or 2 days [LNCaP, **(B)**] with the indicated concentrations of MLN in the presence of 1 μ M CellEvent and stained for 8 h with LysoTracker Deep Red as described in **Figure 3** legend. Bright field and fluorescence images were acquired with the CellInsight NXT HCS platform and analyzed using the Morphology V4 application. The box plots created with “R” software show the changes in spheroid phenotype induced by MLN compared with the mean values in the control spheroids (mean \pm SD, six spheroids per condition, per plate, P -values: *** $<$ 0.001, ** $<$ 0.01, and * $<$ 0.05).

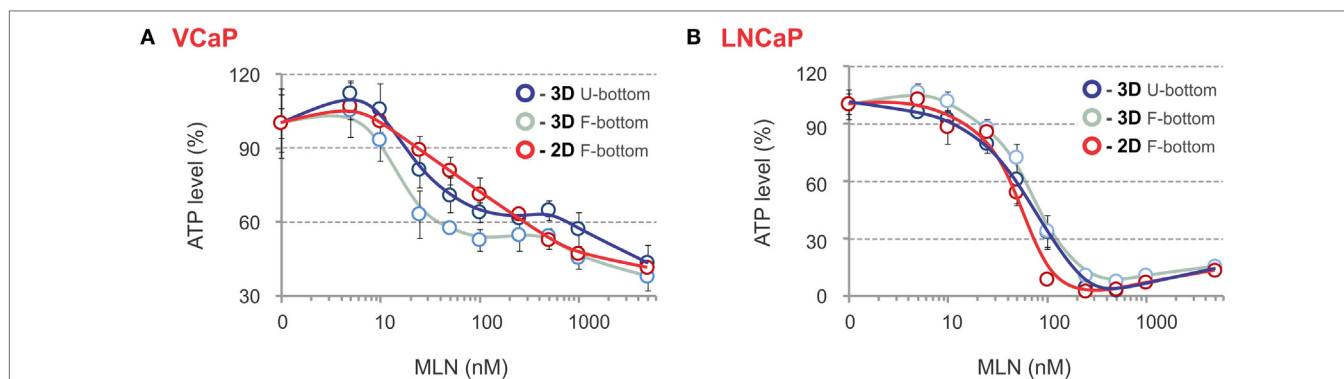


FIGURE 5 | ATP-based endpoint assay to assess the MLN effect. **(A,B)** Spheroids were preformed **(A)** for 7 days with 2,000 VCaP cells and **(B)** for 4 days with 500 LNCaP cells and treated for 4 days (VCaP) or 2 days (LNCaP) with the indicated concentrations of MLN. Then, the spheroids were lysed with Vialight™ reagent, and luminescence was measured directly in the U-bottomed 96-well NTA plate using a GloMax®-Multi Detection System (dark blue curves, 3D U-bottom). Then, the spheroid lysates were transferred into a white plate with a flat transparent bottom (Greiner Bio-One), and luminescence was remeasured (light blue curves, 3D F-bottom). In parallel, VCaP (100,000 cells seeded) and LNCaP (20,000 cells seeded) monolayer cultures in white microtiter plates with a flat transparent bottom (Greiner) were processed similarly with Vialight™ reagent and analyzed (red curves, 2D F-bottom). The data were normalized to the mean value obtained under control conditions (MLN = 0 nM) and are plotted as the means \pm SD (six replicates per condition, per plate).

TABLE 3 | Quantitative evaluation of MLN effect.

	Growth	Integrity	Apoptosis		Viability	Viability		Nedd8
	Area ^a	P2A ^a	3D-CE ^a	2D-CE ^c	LysoT ^a	3D-ATP ^b	2D-ATP ^b	WB ^c
VCaP	18	n/a	20; >600 ^d	500	20; 500 ^d	20; >600 ^d	500	8
LNCaP	18; 190 ^d	250	180	130	70	70	50	10

MLN EC50 values were estimated from dose–response curves and are expressed in nanomolars. For complex dependency graphs, EC50 was determined as the concentration corresponding to the half change in the monitored parameter between the local maximum and local minimum.

P2A, shape P2A; CE, CellEvent; LysoT, LysoTracker Deep Red; WB, western blot.

^aEstimated from the graphs shown in **Figure 4**.

^bEstimated from the graphs shown in **Figure 5**.

^cThe EC50 values for apoptosis stimulation in monolayer cultures and inhibition of neddylation of cellular proteins were estimated from the data in Ref. (77).

^dTwo EC50 values were tentatively assigned to the dose–response curve.

TABLE 4 | Summary of drug responses in VCaP and LNCaP cell lines.

Drug		Growth	Integrity	Apoptosis	Viability	Viability	
		Area ^a	Shape P2A ^a	3D-CE ^a	LysoT ^a	3D-ATP ^b	2D-ATP ^b
Cisplatin (μ M)	VCaP	5	50	5; 25 ^c	50	4; 60 ^c	40
	LNCaP	4	30	4; 30 ^c	30	30	30
Docetaxel (nM)	VCaP	5	1.5	5	5	3	2
	LNCaP	10	2	15	15	15	2
Etoposide (μ M)	VCaP	0.8	5	0.3; 4 ^c	1	1	1
	LNCaP	1	n/a	0.8	1.5	2	2
ARN-509 (nM)	VCaP	80	n/a	400	100	100	150
	LNCaP	13	n/a	15	13	n/a	n/a

EC50 values were estimated from dose–response curves and are expressed in nanomolars (docetaxel and ARN-509) or in micromolars (cisplatin and etoposide). For complex dependency graphs, EC50 was determined as the concentration corresponding to the half change in the monitored parameter between the local maximum and local minimum. CE, CellEvent; LysoT, LysoTracker Deep Red.

^aEstimated from the graphs shown in Figures S2–S5 in Supplementary Material.

^bEstimated from the graphs shown in Figure S6 in Supplementary Material.

^cTwo EC50 values were tentatively assigned to the dose–response curve.

for LNCaP and 4 days for VCaP), cell viability within spheroids was measured with a Vialight ATP-based assay, and the resulting dose–response curves were compared with those obtained with monolayer cultures (Figure S6 in Supplementary Material).

The measured EC50 values are summarized in **Table 4**. The endpoint ATP assay showed that all drugs suppressed cancer cell growth. As often observed in 3D models (101), spheroids showed similar or increased resistance to drug treatments compared

with the corresponding 2D cultures (Figure S6 in Supplementary Material).

High-content analysis (HCA) confirmed complementarity of the morphometric (“Area” vs “Shape P2A”) as well as the fluorescence (“CellEvent” vs “LysoTracker”) phenotypic parameters for characterization of the drug effects (Figures S2–S5 in Supplementary Material). Compared with the ATP assay, an analysis of the phenotypic changes revealed a more complex effect of the drug action. Thus, similar to MLN, the dose–response curves were not always sigmoidal or monotonic (see, for example, CellEvent apoptosis measurements, Figures S2 and S3 in Supplementary Material), which resulted in more than one EC50 value (Table 4). The sign of the effect could also vary depending on the drug. For instance, docetaxel induced an increase in the “Area” parameter in both VCaP and LNCaP spheroids, while all other drug treatments reduced the spheroid size (Figures S2–S5 in Supplementary Material). Furthermore, the obtained EC50 values differed, sometimes significantly, from those measured with the ATP-endpoint assay and often were smaller.

To summarize the HCA results, we plotted all EC50 values measured for a particular drug on the same diagram (Figure 6). Because up to two EC50s could be observed for each phenotypic parameter, the increments “–1” and “–2” were used to indicate lower and higher value, respectively. For each cell line, we traced a “static” threshold line that corresponded to the drug concentration at which no change in spheroid ATP content was observed within a given treatment time [2 days for LNCaP (red line) and 4 days for VCaP (green line)]. Using these thresholds, the observed EC50 values were tentatively assigned to cytostatic (value below threshold) or cytotoxic (above threshold) drug action. As a result, some treatments appeared mostly cytostatic (etoposide and ARN-509 in both cell lines, docetaxel in LNCaP), whereas others showed a concentration-dependent cytostatic-to-cytotoxic transition (cisplatin and MLN in both cell lines) or purely cytotoxic effect (docetaxel in VCaP) (Figure 6).

It should be noted that conditions underlying spheroid growth arrest were different depending on the drug. Thus, the cytostatic effect of low doses of MLN in VCaP and etoposide in LNCaP spheroids was characterized by stabilization of spheroid size, a slight increase in mean LysoTracker fluorescence and

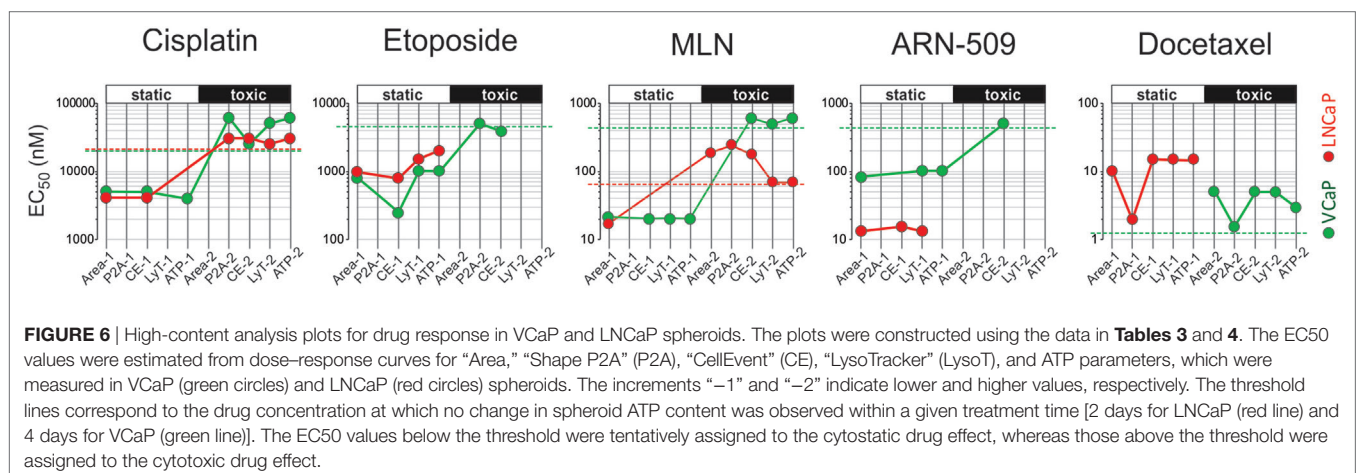
the absence of drug-induced apoptosis (Figures 7A,B). The formation of an apoptotic spheroid core was also completely prevented. As we previously showed for MLN, this rather stable quiescent state resulted from G0/G1 cell cycle arrest and could be reversible (77). By contrast, etoposide treatment of VCaP or docetaxel treatment of LNCaP spheroids was characterized by a significant apoptosis rate (Figures 7A,B). Many apoptotic cells were localized on the periphery and in protruding blebs. This suggests that the apparent cytostatic state was a result of a stationary equilibrium between cell proliferation and expulsion of dying cells, as it was previously described for tissue-derived colospheres and organotypic multicellular spheroids (5). This condition seems transient because extension of docetaxel treatment to 4 days resulted in a significant decline in viability of LNCaP spheroids, similar to that observed in VCaP cells.

Finally, despite the observation that the cytotoxic effects of different drugs shared many common characteristics, i.e., ATP decline, apoptosis, decrease in LysoTracker uptake, and compromised integrity (increase in “Shape P2A”), the corresponding spheroid phenotypes were very distinct (Figures 7C,D). This difference apparently reflects a particular MOA of the drugs. As a result, spheroids formed by different cell lines but treated with the same drug had greater resemblance than spheroids formed by the same cell line but treated with different drugs (see, for example, the characteristic “halo” of apoptotic cells in docetaxel-treated spheroids, Figures 7C,D). In our study, the most striking example of the unique drug effects was the asymmetric unilateral spheroid disruption seen in almost all LNCaP spheroids treated with 500 nM MLN (Figures 2D, 3D and 7D).

DISCUSSION

Recent technological developments have renewed an interest in spheroid culture as a pertinent model for drug screening. However, although the availability of spheroid-specific consumables and high-content imaging platforms promises to make spheroid analysis easier, it remains far from routine in many laboratories.

We describe a method that allows easy and straightforward generation of uniform multicellular spheroids, their staining with vital dyes, real-time monitoring of the drug effect, and endpoint



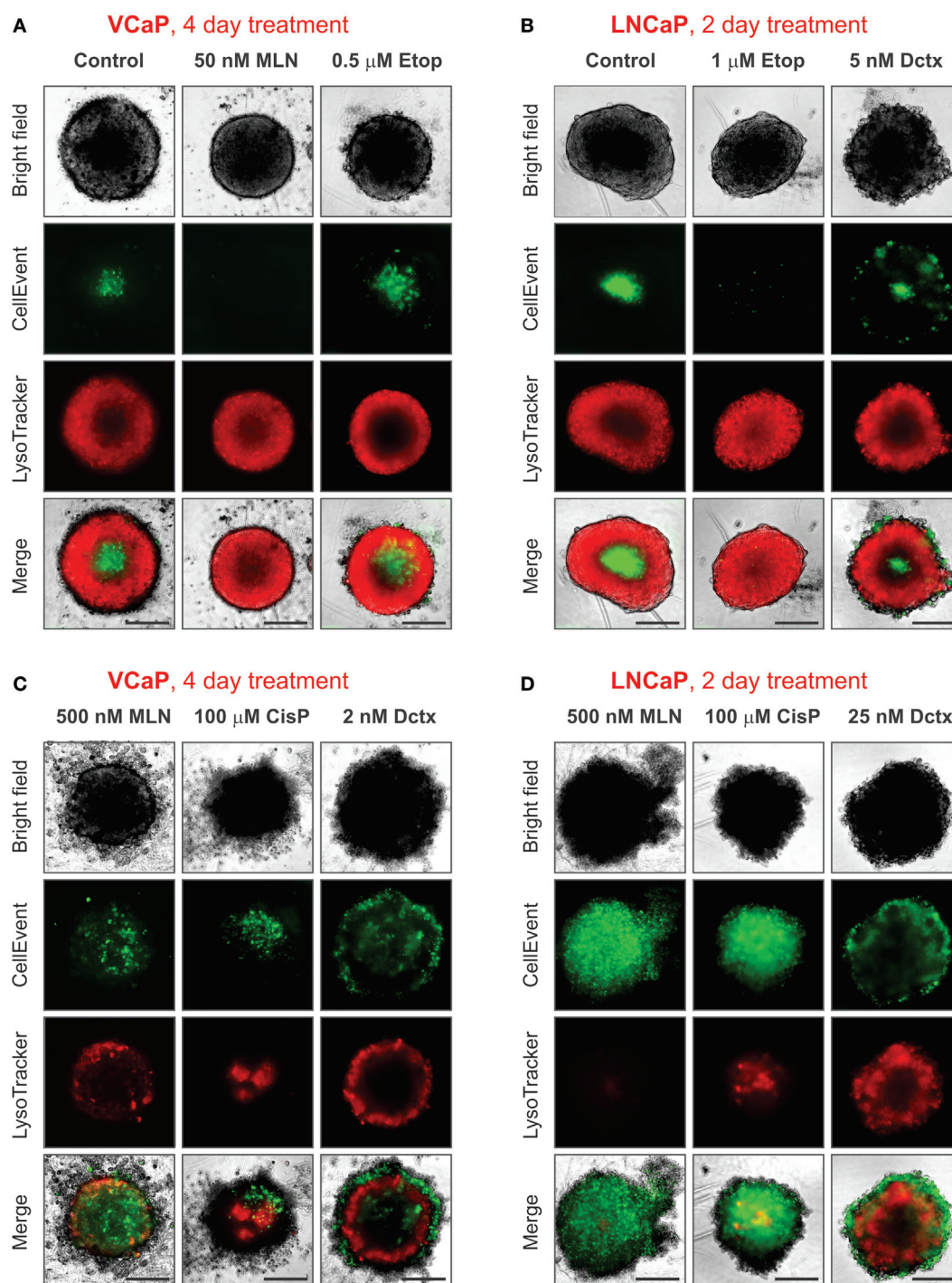


FIGURE 7 | Various phenotypes of drug-treated spheroids. The experimental conditions were the same as described in **Figure 3** legend. **(A,B)** Distinct cytosstatic phenotypes. **(C,D)** Distinct cytosotoxic phenotypes. Scale bar, 200 μ m.

viability assays to be performed sequentially in the same 96-well microtiter plate. To demonstrate the method performance, we used inexpensive NTA plates (instead of ULA plates) that, nevertheless, ensured robust spheroid generation and analysis. Furthermore, although we used the CellInsight HCS platform,

spheroid imaging can also be performed on standard or lens free (92) microscopes and analyzed using open-source tools, e.g., based on MATLAB (39), ImageJ (83), or Fiji (93).

There are several points to consider with the use of Falcon[®]96 Non-Treated Assay Plates (#353910). First, among the various

non-treated polystyrene plates we examined, these plates performed the best in spheroid formation. Second, the plates are supplied non-sterile in peel-open medical-style packaging. Although we never had contamination problems when using standard antibiotic-supplemented media (for up to 3 months of spheroid culturing), some antibiotic-sensitive applications, e.g., DNA or siRNA transfection, may require plate sterilization. In our laboratory, a 30-min UV sterilization protocol (102) works well, although sterilization by gas or γ -irradiation can also be used when available. Third, the plates are supplied without lids and can be covered by any lids matching standard 96-well plates, such as those supplied by Thermo (# 5500). Finally, not all cell lines form spheroids in NTA plates. For cell lines, such as PC3, that form only loose aggregates (**Figure 1A**; Figure S1 in Supplementary Material), supplementation of the culture medium with extracellular matrix components can help promote spheroid assembly (21, 33, 103). For immortalized RWPE-1 prostate cells, which do not form spheroids because they are able to attach to a non-treated polystyrene surface and grow in a monolayer, addition of 10% FBS enables efficient spheroid formation (Figure S1 in Supplementary Material). For other cell lines, such as PNT2 and DU145, the use of ULA plates may be preferable.

When performing long-term spheroid monitoring, special attention must be paid to cell seeding density and growth rate. These two parameters determine spheroid size and total imaging time. The optimal spheroid size depends on the assay requirements, e.g., the presence or not of a hypoxic core and optimal fluorescence staining, but is usually within a 200–500 μm diameter range (21, 31, 83). The size is also limited by the instrument imaging capacity. Thus, with acquisition of one field of view per well (896.6 $\mu\text{m} \times 896.6 \mu\text{m}$ for a 10 \times objective on CellInsight NXT), the diameter of spheroids should not exceed 800 μm . Considering that spheroids are not always perfectly centered within the wells and that spheroids disrupted by drugs may have an irregular shape (**Figures 2D** and **3D**), this size limit may be even smaller (<600 μm).

Furthermore, large spheroids have more significant molecular (nutrient, metabolite, drug, probe, etc.) gradients that can affect the apparent phenotypic outcome of the drug treatment. For example, the CellEvent apoptotic signal produced by the hypoxic core of a fast-growing spheroid (>450 μm in diameter) may be comparable or even greater than that induced by a drug, thus interfering with cytotoxicity measurement. In such cases, analysis of smaller spheroids may be preferable.

Although spheroid size and shape remain the primary parameters for real-time monitoring of a drug effect (21, 38, 39), the use of fluorescent probes provides additional information regarding the mechanism of drug action (20, 23, 47, 48). In principle, the more probes you use, the more information you gather. However, the probes should not interfere with spheroid growth, the drug effect or each other. Here, we show that the use of CellEvent and LysoTracker Deep Red ensures independent real-time monitoring of the MLN effect on spheroid viability and cell apoptosis. Combined with the morphometric analysis and ATP-based endpoint viability assay, this allows for the complex effect of the drug action to be described in a series of EC50 values (**Tables 3** and **4**; **Figure 6**).

CONCLUDING REMARKS

In recent years, significant efforts have been made to implement 3D models in drug discovery protocols (1, 101, 104). The hope is that using 3D models will result in more efficient selection of drug candidates and diminish the rate of drug attrition. Indeed, the transition from monolayer culture to a more natural 3D context can significantly alter the response of cancer cells to chemotherapeutics. Generally, cancer cells cultured in 3D systems become more refractory to various treatments due to limited drug penetration and activation of numerous resistance mechanisms, although the opposite has also been observed [see Ref. (101, 104) for review]. Consequently, many reports have focused on the difference in drug cytotoxicity in various cancer models (46, 74, 105–107). Beyond the cytotoxicity issue, 3D models have also been applied to discover molecules that suppress tumor-relevant processes, such as hypoxia-induced drug resistance (23), metastasis-like invasion and cancer cell spreading (21), and cancer-associated fibroblast infiltration (20). Often, analysis of complex phenotypes requires high-content monitoring of multiple parameters. For example, HCA coupled with an advanced image treatment has been successfully performed in a semi-automated manner on heterogeneous matrix-embedded 3D cultures (108–110). Such analysis is significantly simplified when an array of uniform spheroids that allows reproducible detection of fine changes in specific cellular phenotype is used (20, 23, 47–49). Thus, the effect of drugs on multiple cellular processes, such as mitochondria function, apoptosis, and cell homeostasis, can be followed using specific fluorescent probes (**Table 2**) with a high level of confidence.

In this report, we demonstrate that simultaneous monitoring of two morphometric and two fluorescence parameters permits clear discrimination between cytostatic and cytotoxic drug effects. This may be particularly pertinent for preclinical evaluation of drug effects, because cytostatic conditions are often implicated in tumor dormancy, drug resistance, and development of more aggressive phenotypes (111, 112). Compared with monolayer cultures, monitoring of 3D phenotypic parameters, such as spheroid size, shape, and internal organization report on “macroscopic” effects of drug treatment. Numerous studies have reported that different drugs induce quite distinct spheroid phenotypes (23, 47, 48). We observed that docetaxel and MLN produced characteristic changes in spheroid morphology that likely reflect a particular mechanism of drug action. Detailed characterization of a drug-induced phenotype may therefore help in evaluating the outcomes of drug actions on a multicellular/tissue level. In this context, and for future development of the method, 3D-confocal imaging can be used to enable efficient 3D reconstruction of spheroid phenotypes *via* z-stacking and subsequent 3D convolution (47, 113). We believe that once fully validated in a wider range of conditions the method described here could be particularly valuable for phenotype-based drug discovery (114–116).

AUTHOR CONTRIBUTIONS

FM and PO performed most of the data acquisition and analysis and participated in designing the experiments and writing

the manuscript. AR and VH performed some of the experiments and participated in data analysis and the writing of the manuscript. XG provided conceptual input and participated in data analysis and the writing of the manuscript. MB designed and supervised the experiments, analyzed the data, and wrote the manuscript.

ACKNOWLEDGMENTS

The authors are grateful to Monika E. Dolega, who performed preliminary screening of commercial U-bottom plates and wrote one of the ImageJ macros used for spheroid analysis.

REFERENCES

- Horvath P, Aulner N, Bickle M, Davies AM, Nery ED, Ebner D, et al. Screening out irrelevant cell-based models of disease. *Nat Rev Drug Discov* (2016) 15(11):751–69. doi:10.1038/nrd.2016.175
- Scannell JW, Blanckley A, Boldon H, Warrington B. Diagnosing the decline in pharmaceutical R&D efficiency. *Nat Rev Drug Discov* (2012) 11(3):191–200. doi:10.1038/nrd3681
- Allison M. Reinventing clinical trials. *Nat Biotechnol* (2012) 30(1):41–9. doi:10.1038/nbt.2083
- Hirschhaeuser F, Menne H, Dittfeld C, West J, Mueller-Klieser W, Kunz-Schughart LA. Multicellular tumor spheroids: an underestimated tool is catching up again. *J Biotechnol* (2010) 148(1):3–15. doi:10.1016/j.jbiotec.2010.01.012
- Weiswald LB, Bellet D, Dangles-Marie V. Spherical cancer models in tumor biology. *Neoplasia* (2015) 17(1):1–15. doi:10.1016/j.neo.2014.12.004
- Bredenoord AL, Clevers H, Knoblich JA. Human tissues in a dish: the research and ethical implications of organoid technology. *Science* (2017) 355(6322):eaaf9414. doi:10.1126/science.aaf9414
- Fatehullah A, Tan SH, Barker N. Organoids as an in vitro model of human development and disease. *Nat Cell Biol* (2016) 18(3):246–54. doi:10.1038/ncb3312
- Lancaster MA, Knoblich JA. Organogenesis in a dish: modeling development and disease using organoid technologies. *Science* (2014) 345(6194):1247125. doi:10.1126/science.1247125
- Esch EW, Bahinski A, Huh D. Organs-on-chips at the frontiers of drug discovery. *Nat Rev Drug Discov* (2015) 14(4):248–60. doi:10.1038/nrd4539
- Skardal A, Shupe T, Atala A. Organoid-on-a-chip and body-on-a-chip systems for drug screening and disease modeling. *Drug Discov Today* (2016) 21(9):1399–411. doi:10.1016/j.drudis.2016.07.003
- Pati F, Gantelius J, Svahn HA. 3D bioprinting of tissue/organ models. *Angew Chem Int Ed Engl* (2016) 55(15):4650–65. doi:10.1002/anie.201505062
- Nath S, Devi GR. Three-dimensional culture systems in cancer research: focus on tumor spheroid model. *Pharmacol Ther* (2016) 163:94–108. doi:10.1016/j.pharmthera.2016.03.013
- Thoma CR, Zimmermann M, Agarkova I, Kelm JM, Krek W. 3D cell culture systems modeling tumor growth determinants in cancer target discovery. *Adv Drug Deliv Rev* (2014) 6(9–70):29–41. doi:10.1016/j.addr.2014.03.001
- Jedrzejczak-Silicka M. Chapter 1: History of cell culture. In: S. Joghi Thatha Gowder, editor. *Biochemistry, Genetics and Molecular Biology. New Insights into Cell Culture Technology* (2017). Available from: <https://www.intechopen.com/books/new-insights-into-cell-culture-technology/history-of-cell-culture>
- Rodríguez-Hernández CO, Torres-García SE, Olvera-Sandoval C, Ramírez-Castillo FY, Muro AL, Avelar-Gonzalez FJ, et al. Cell culture: history, development and prospects. *Int J Curr Res Aca Rev* (2014) 2(12):188–200.
- Harrison RG. Observations on the living developing nerve fiber. *Anat Rec* (1907) 5:116–28. doi:10.1002/ar.1090010503
- Moscona A. The development in vitro of chimeric aggregates of dissociated embryonic chick and mouse cells. *Proc Natl Acad Sci U S A* (1957) 43(1):184–94. doi:10.1073/pnas.43.1.184
- Sutherland RM, McCredie JA, Inch WR. Growth of multicell spheroids in tissue culture as a model of nodular carcinomas. *J Nat Cancer Inst* (1971) 46:113–20.
- Comley J. Spheroids rapidly becoming a preferred 3D culture format. *Drug Discov World* (2017) 15:31–49.
- Wenzel C, Otto S, Prechtel S, Parczyk K, Steigemann P. A novel 3D high-content assay identifies compounds that prevent fibroblast invasion into tissue surrogates. *Exp Cell Res* (2015) 339(1):35–43. doi:10.1016/j.yexcr.2015.10.003
- Vinci M, Gowan S, Boxall F, Patterson L, Zimmermann M, Court W, et al. Advances in establishment and analysis of three-dimensional tumor spheroid-based functional assays for target validation and drug evaluation. *BMC Biol* (2012) 10:29. doi:10.1186/1741-7007-10-29
- Friedrich J, Seidel C, Ebner R, Kunz-Schughart LA. Spheroid-based drug screen: considerations and practical approach. *Nat Protoc* (2009) 4(3):309–24. doi:10.1038/nprot.2008.226
- Wenzel C, Riefke B, Gründemann S, Krebs A, Christian S, Prinz F, et al. 3D high-content screening for the identification of compounds that target cells in dormant tumor spheroid regions. *Exp Cell Res* (2014) 323(1):131–43. doi:10.1016/j.yexcr.2014.01.017
- Astashkina A, Grainger DW. Critical analysis of 3-D organoid in vitro cell culture models for high-throughput drug candidate toxicity assessments. *Adv Drug Deliv Rev* (2014) 6(9–70):1–18. doi:10.1016/j.addr.2014.02.008
- Wartenberg M, Dönmez F, Ling FC, Acker H, Hescheler J, Sauer H. Tumor-induced angiogenesis studied in confrontation cultures of multicellular tumor spheroids and embryoid bodies grown from pluripotent embryonic stem cells. *FASEB J* (2001) 15(6):995–1005. doi:10.1096/fj.00-0350com
- Kelm JM, Timmins NE, Brown CJ, Fussenegger M, Nielsen LK. Method for generation of homogeneous multicellular tumor spheroids applicable to a wide variety of cell types. *Biotechnol Bioeng* (2003) 83(2):173–80. doi:10.1002/bit.10655
- Haisler WL, Timm DM, Gage JA, Tseng H, Killian TC, Souza GR. Three-dimensional cell culturing by magnetic levitation. *Nat Protoc* (2013) 8(10):1940–9. doi:10.1038/nprot.2013.125
- Ingram M, Techy GB, Saroufem R, Yazan O, Narayan KS, Goodwin TJ, et al. Three-dimensional growth patterns of various human tumor cell lines in simulated microgravity of a NASA bioreactor. *In Vitro Cell Dev Biol Anim* (1997) 33(6):459–66. doi:10.1007/s11626-997-0064-8
- Debnath J, Muthuswamy SK, Brugge JS. Morphogenesis and oncogenesis of MCF-10A mammary epithelial acini grown in three-dimensional basement membrane cultures. *Methods* (2003) 30(3):256–68. doi:10.1016/S1046-2023(03)00032-X
- Lang SH, Sharrard RM, Stark M, Villette JM, Maitland NJ. Prostate epithelial cell lines form spheroids with evidence of glandular differentiation in three-dimensional Matrigel cultures. *Br J Cancer* (2001) 85(4):590–9. doi:10.1054/bjoc.2001.1967
- Fischbach C, Chen R, Matsumoto T, Schmelzle T, Brugge JS, Polverini PJ, et al. Engineering tumors with 3D scaffolds. *Nat Methods* (2007) 4(10):855–60. doi:10.1038/nmeth1085

SUPPLEMENTARY MATERIAL

The Supplementary Material for this article can be found online at <http://www.frontiersin.org/article/10.3389/fonc.2017.00293/full#supplementary-material>.

VIDEO S1 | VCaP spheroid assembly.

32. Yuhas JM, Li AP, Martinez AO, Ladman AJ. A simplified method for production and growth of multicellular tumor spheroids. *Cancer Res* (1977) 37(10):3639–43.
33. Ivascu A, Kubbies M. Rapid generation of single-tumor spheroids for high-throughput cell function and toxicity analysis. *J Biomol Screen* (2006) 11(8):922–32. doi:10.1177/1087057106292763
34. Koide N, Sakaguchi K, Koide Y, Asano K, Kawaguchi M, Matsushima H, et al. Formation of multicellular spheroids composed of adult rat hepatocytes in dishes with positively charged surfaces and under other nonadherent environments. *Exp Cell Res* (1990) 186(2):227–35. doi:10.1016/0014-4827(90)90300-Y
35. Curtis AS, Forrester JV, McInnes C, Lawrie F. Adhesion of cells to polystyrene surfaces. *J Cell Biol* (1983) 97(5 Pt 1):1500–6. doi:10.1083/jcb.97.5.1500
36. Ramsey WS, Hertl W, Nowlan ED, Binkowski NJ. Surface treatments and cell attachment. *In Vitro* (1984) 20(10):802–8. doi:10.1007/BF02618296
37. Freyer JP, Sutherland RM. Selective dissociation and characterization of cells from different regions of multicell tumor spheroid. *Cancer Res* (1980) 40(11):3956–65.
38. Baek N, Seo OW, Kim M, Hulme J, An SS. Monitoring the effects of doxorubicin on 3D-spheroid tumor cells in real-time. *Onco Targets Ther* (2016) 9:7207–18. doi:10.2147/OTT.S112566
39. Zanoni M, Piccinini F, Arienti C, Zamagni A, Santi S, Polico R, et al. 3D tumor spheroid models for in vitro therapeutic screening: a systematic approach to enhance the biological relevance of data obtained. *Sci Rep* (2016) 6:19103. doi:10.1038/srep19103
40. Vinci M, Box C, Eccles SA. Three-dimensional (3D) tumor spheroid invasion assay. *J Vis Exp* (2015) (99):e52686. doi:10.3791/52686
41. Smyrek I, Stelzer EH. Quantitative three-dimensional evaluation of immunofluorescence staining for large whole mount spheroids with light sheet microscopy. *Biomed Opt Express* (2017) 8(2):484–99. doi:10.1364/BOE.8.000484
42. Dufau I, Frongia C, Sicard F, Dedieu L, Cordelier P, Ausseil F, et al. Multicellular tumor spheroid model to evaluate spatio-temporal dynamics effect of chemotherapeutics: application to the gemcitabine/CHK1 inhibitor combination in pancreatic cancer. *BMC Cancer* (2012) 12:15. doi:10.1186/1471-2407-12-15
43. Weiswald LB, Guinebretière JM, Richon S, Bellet D, Saubaméa B, Dangles-Marie V. In situ protein expression in tumour spheres: development of an immunostaining protocol for confocal microscopy. *BMC Cancer* (2010) 10(1):106. doi:10.1186/1471-2407-10-106
44. Anastasov N, Höfig I, Radulović V, Ströbel S, Salomon M, Lichtenberg J, et al. A 3D-microtissue-based phenotypic screening of radiation resistant tumor cells with synchronized chemotherapeutic treatment. *BMC Cancer* (2015) 15:466. doi:10.1186/s12885-015-1481-9
45. Martinez NJ, Titus SA, Wagner AK, Simeonov A. High-throughput fluorescence imaging approaches for drug discovery using in vitro and in vivo three-dimensional models. *Expert Opin Drug Discov* (2015) 10(12):1347–61. doi:10.1517/17460441.2015.1091814
46. Stock K, Estrada MF, Vidic S, Gjerde K, Rudisch A, Santo VE, et al. Capturing tumor complexity in vitro: comparative analysis of 2D and 3D tumor models for drug discovery. *Sci Rep* (2016) 6:28951. doi:10.1038/srep28951
47. Sirenko O, Mitlo T, Hesley J, Luke S, Owens W, Cromwell EF. High-content assays for characterizing the viability and morphology of 3D cancer spheroid cultures. *Assay Drug Dev Technol* (2015) 13(7):402–14. doi:10.1089/adt.2015.655
48. Sirenko O, Hancock MK, Hesley J, Hong D, Cohen A, Gentry J, et al. Phenotypic characterization of toxic compound effects on liver spheroids derived from iPSC using confocal imaging and three-dimensional image analysis. *Assay Drug Dev Technol* (2016) 14(7):381–94. doi:10.1089/adt.2016.729
49. Arora J, Sauer SJ, Tarpley M, Vermeulen P, Rypens C, Van Laere S, et al. Inflammatory breast cancer tumor emboli express high levels of anti-apoptotic proteins: use of a quantitative high content and high-throughput 3D IBC spheroid assay to identify targeting strategies. *Oncotarget* (2017) 8(16):25848. doi:10.18632/oncotarget.15667
50. Curran S, Vantagoli MM, Boekelheide K, Morgan JR. Architecture of chimeric spheroids controls drug transport. *Cancer Microenviron* (2015) 8(2):101–9. doi:10.1007/s12307-015-0171-0
51. Yoshida T, Okuyama H, Nakayama M, Endo H, Nonomura N, Nishimura K, et al. High-dose chemotherapeutics of intravesical chemotherapy rapidly induce mitochondrial dysfunction in bladder cancer-derived spheroids. *Cancer Sci* (2015) 106(1):69–77. doi:10.1111/cas.12567
52. Ravenscroft S, Bauch C, Hinton L, Walke P. *Microtissues for In Vitro Toxicity Assessment: Cost Effective and In Vivo Relevant Toxicology Tools*. Drug Discovery World (2016). p. 68–74.
53. Larson B, Banks P, Hunt S, Moeller T, Long D. *The Impact of a 3-Dimensional Human Liver Microtissue Model on Long-term Hepatotoxicity Studies*. BioTek-Application Note (2014). Available from: https://www.biotek.com/assets/tech_resources/InSphero_App_Note_FINAL.pdf
54. Swoger J, Pampaloni F, Stelzer EH. Imaging cellular spheroids with a single (selective) plane illumination microscope. *Cold Spring Harb Protoc* (2014) 2014(1):106–13. doi:10.1101/pdb.prot080176
55. Trumpi K, Egan DA, Vellinga TT, Borel Rinkes IH, Kranenburg O. Paired image- and FACS-based toxicity assays for high content screening of spheroid-type tumor cell cultures. *FEBS Open Bio* (2015) 5:85–90. doi:10.1016/j.fob.2015.01.003
56. Wylie PG, Onley DJ, Hammerstein AF, Bowen WP. Advances in laser scanning imaging cytometry for high-content screening. *Assay Drug Dev Technol* (2015) 13(2):66–78. doi:10.1089/adt.2014.607
57. Hsiao AY, Tung YC, Qu X, Patel LR, Pienta KJ, Takayama S. 384 hanging drop arrays give excellent Z-factors and allow versatile formation of co-culture spheroids. *Biotechnol Bioeng* (2012) 109(5):1293–304. doi:10.1002/bit.24399
58. Beauchamp P, Moritz W, Kelm JM, Ullrich ND, Agarkova I, Anson BD, et al. Development and characterization of a scaffold-free 3D spheroid model of induced pluripotent stem cell-derived human cardiomyocytes. *Tissue Eng Part C Methods* (2015) 21(8):852–61. doi:10.1089/ten.TEC.2014.0376
59. Yip D, Cho CH. A multicellular 3D heterospheroid model of liver tumor and stromal cells in collagen gel for anti-cancer drug testing. *Biochem Biophys Res Commun* (2013) 433(3):327–32. doi:10.1016/j.bbrc.2013.03.008
60. Xiao L, Kumazawa Y, Okamura H. Cell death, cavitation and spontaneous multi-differentiation of dental pulp stem cells-derived spheroids in vitro: a journey to survival and organogenesis. *Biol Cell* (2014) 106(12):405–19. doi:10.1111/boc.201400024
61. Achilli TM, McCalla S, Meyer J, Tripathi A, Morgan JR. Multilayer spheroids to quantify drug uptake and diffusion in 3D. *Mol Pharm* (2014) 11(7):2071–81. doi:10.1021/mp500002y
62. Kasinskas RW, Venkatasubramanian R, Forbes NS. Rapid uptake of glucose and lactate, and not hypoxia, induces apoptosis in three-dimensional tumor tissue culture. *Integr Biol* (2014) 6(4):399–410. doi:10.1039/C4IB00001C
63. Solomon MA, Lamera J, D'Souza GG. Development of an in vitro tumor spheroid culture model amenable to high-throughput testing of potential anti-cancer nanotherapeutics. *J Liposome Res* (2016) 26(3):246–60. doi:10.3109/08982104.2015.1105820
64. Colak S, Zimmerlin CD, Fessler E, Hogdal L, Prasetyanti PR, Grandela CM, et al. Decreased mitochondrial priming determines chemoresistance of colon cancer stem cells. *Cell Death Differ* (2014) 21(7):1170–7. doi:10.1038/cdd.2014.37
65. Herroon MK, Diedrich JD, Podgorski I. New 3D-culture approaches to study interactions of bone marrow adipocytes with metastatic prostate cancer cells. *Front Endocrinol* (2016) 7:84. doi:10.3389/fendo.2016.00084
66. Jenkins J, Borisov SM, Papkovsky DB, Dmitriev RI. Sulforhodamine nanothermometer for multiparametric fluorescence lifetime imaging microscopy. *Anal Chem* (2016) 88(21):10566–72. doi:10.1021/acs.analchem.6b02675
67. Fomin MA, Dmitriev RI, Jenkins J, Papkovsky DB, Heindl D, König B. Two-acceptor cyanine-based fluorescent indicator for NAD(P)H in tumor cell models. *ACS Sens* (2016) 1(6):702–9. doi:10.1021/acssensors.5b00315
68. Vamvakidou AP, Mondrinos MJ, Petushi SP, Garcia FU, Lelkes PI, Tozeren A. Heterogeneous breast tumoroids: an in vitro assay for investigating cellular heterogeneity and drug delivery. *J Biomol Screen* (2007) 12(1):13–20. doi:10.1177/1087057106296482
69. Ivanov DP, Parker TL, Walker DA, Alexander C, Ashford MB, Gellert PR, et al. In vitro co-culture model of medulloblastoma and human neural stem cells for drug delivery assessment. *J Biotechnol* (2015) 205:3–13. doi:10.1016/j.jbiotec.2015.01.002
70. Mori H, Ninomiya K, Kino-oka M, Shofuda T, Islam MO, Yamasaki M, et al. Effect of neurosphere size on the growth rate of human neural

- stem/progenitor cells. *J Neurosci Res* (2006) 84(8):1682–91. doi:10.1002/jnr.21082
71. Waschow M, Letsch S, Böttcher K, Kelm JM. High-content analysis of biomarker intensity and distribution in 3D microtissues. *Nat Methods* (2012) 9:iii–v.
 72. McKenna N. Cellular models for finer screening. *Genet Eng Biotechnol News* (2014) 34(8):30–3. doi:10.1089/gen.34.08.15
 73. Larson B, Hunt S, Luty W, Banks P. *PMT and Image-Based Analysis of Hypoxia Induction Using a 3D Spheroid Model*. ENZO Life Sci Application Note (2015).
 74. Imamura Y, Mukohara T, Shimono Y, Funakoshi Y, Chayahara N, Toyoda M, et al. Comparison of 2D- and 3D-culture models as drug-testing platforms in breast cancer. *Oncol Rep* (2015) 33(4):1837–43. doi:10.3892/or.2015.3767
 75. Yoshii Y, Furukawa T, Waki A, Okuyama H, Inoue M, Itoh M, et al. High-throughput screening with nanoimprinting 3D culture for efficient drug development by mimicking the tumor environment. *Biomaterials* (2015) 51:278–89. doi:10.1016/j.biomaterials.2015.02.008
 76. Cheng G, Tse J, Jain RK, Munn LL. Micro-environmental mechanical stress controls tumor spheroid size and morphology by suppressing proliferation and inducing apoptosis in cancer cells. *PLoS One* (2009) 4(2):e4632. doi:10.1371/journal.pone.0004632
 77. Rulina AV, Mittler F, Obeid P, Gerbaud S, Guyon L, Sulpice E, et al. Distinct outcomes of CRL–Nedd8 pathway inhibition reveal cancer cell plasticity. *Cell Death Dis* (2016) 7(12):e2505. doi:10.1038/cddis.2016.395
 78. Fogel JL, Thein TZ, Mariani FV. Use of LysoTracker to detect programmed cell death in embryos and differentiating embryonic stem cells. *J Vis Exp* (2012) (68):4254. doi:10.3791/4254
 79. Espina V, Mariani BD, Gallagher RI, Tran K, Banks S, Wiedemann J, et al. Malignant precursor cells pre-exist in human breast DCIS and require autophagy for survival. *PLoS One* (2010) 5(4):e10240. doi:10.1371/journal.pone.0010240
 80. Takagi M, Sanoh S, Santoh M, Ejiri Y, Kotake Y, Ohta S. Detection of metabolic activation leading to drug-induced phospholipidosis in rat hepatocyte spheroids. *J Toxicol Sci* (2016) 41(1):155–64. doi:10.2131/jts.41.155
 81. Ho WY, Yeap SK, Ho CL, Rahim RA, Alitheen NB. Development of multicellular tumor spheroid (MCTS) culture from breast cancer cell and a high throughput screening method using the MTT assay. *PLoS One* (2012) 7(9):e44640. doi:10.1371/journal.pone.0044640
 82. Friedrich J, Eder W, Castaneda J, Doss M, Huber E, Ebner R, et al. A reliable tool to determine cell viability in complex 3-D culture: the acid phosphatase assay. *J Biomol Screen* (2007) 12(7):925–37. doi:10.1177/1087057107306839
 83. Ivanov DP, Parker TL, Walker DA, Alexander C, Ashford MB, Gellert PR, et al. Multiplexing spheroid volume, resazurin and acid phosphatase viability assays for high-throughput screening of tumour spheroids and stem cell neurospheres. *PLoS One* (2014) 9(8):e103817. doi:10.1371/journal.pone.0103817
 84. Xiao J, Zhang Y, Wang J, Yu W, Wang W, Ma X. Monitoring of cell viability and proliferation in hydrogel-encapsulated system by resazurin assay. *Appl Biochem Biotechnol* (2010) 162(7):1996–2007. doi:10.1007/s12010-010-8975-3
 85. Kijanska M, Kelm J. In vitro 3D spheroids and microtissues: ATP-based cell viability and toxicity assays. In: Sittampalam GS, Coussens NP, Brimacombe K, editors. *Assay Guidance Manual*. Bethesda, MD: Eli Lilly & Company and the National Center for Advancing Translational Sciences (2016). p. 1–16.
 86. Walzl A, Unger C, Kramer N, Unterleuthner D, Scherzer M, Hengstschläger M, et al. The resazurin reduction assay can distinguish cytotoxic from cytostatic compounds in spheroid screening assays. *J Biomol Screen* (2014) 19(7):1047–59. doi:10.1177/1087057114532352
 87. Soucy TA, Smith PG, Milhollen MA, Berger AJ, Gavin JM, Adhikari S, et al. An inhibitor of NEDD8-activating enzyme as a new approach to treat cancer. *Nature* (2009) 458(7239):732–6. doi:10.1038/nature07884
 88. Sarantopoulos J, Shapiro GI, Cohen RB, Clark JW, Kauh JS, Weiss GJ, et al. Phase I study of the investigational NEDD8-activating enzyme inhibitor pevonedistat (TAK-924/MLN4924) in patients with advanced solid tumors. *Clin Cancer Res* (2016) 22(4):847–57. doi:10.1158/1078-0432.CCR-15-1338
 89. Shah JJ, Jakubowiak AJ, O'Connor OA, Orlowski RZ, Harvey RD, Smith MR, et al. Phase I study of the novel investigational NEDD8-activating enzyme inhibitor pevonedistat (MLN4924) in patients with relapsed/refractory multiple myeloma or lymphoma. *Clin Cancer Res* (2016) 22(1):34–43. doi:10.1158/1078-0432.CCR-15-1237
 90. Lee YG, Korenchuk S, Lehr J, Whitney S, Vessela R, Pienta KJ. Establishment and characterization of a new human prostatic cancer cell line: DuCaP. *In Vivo* (2001) 15(2):157–62.
 91. Ungrin MD, Joshi C, Nica A, Bauwens C, Zandstra PW. Reproducible, ultra high-throughput formation of multicellular organization from single cell suspension-derived human embryonic stem cell aggregates. *PLoS One* (2008) 3(2):e1565. doi:10.1371/journal.pone.0001565
 92. Haguët V, Obeid P, Griffin R, Freida D, Guyon L, Gidrol X. Time-lapse screening by parallelized lensfree imaging. *Proceedings of the 17th International Conference on Miniaturized Systems for Chemistry and Life Sciences (MicroTAS)*. Freiburg, Germany (2013). p. 1740–2.
 93. Schindelin J, Arganda-Carreras I, Frise E, Kaynig V, Longair M, Pietzsch T, et al. Fiji: an open-source platform for biological-image analysis. *Nat Methods* (2012) 9(7):676–82. doi:10.1038/nmeth.2019
 94. Yi YW, Bae I. Effects of solvents on in vitro potencies of platinum compounds. *DNA Repair (Amst)* (2011) 10(11):1084–5. doi:10.1016/j.dnarep.2011.09.008
 95. Hedlund TE, Duke RC, Miller GJ. Three-dimensional spheroid cultures of human prostate cancer cell lines. *Prostate* (1999) 41(3):154–65. doi:10.1002/(SICI)1097-0045(19991101)41:3<154::AID-PROS2>3.0.CO;2-M
 96. Milhollen MA, Narayanan U, Soucy TA, Veiby PO, Smith PG, Amidon B. Inhibition of NEDD8-activating enzyme induces rereplication and apoptosis in human tumor cells consistent with deregulating CDT1 turnover. *Cancer Res* (2011) 71(8):3042–51. doi:10.1158/0008-5472.CAN-10-2122
 97. Pienta KJ, Smith DC. Advances in prostate cancer chemotherapy: a new era begins. *CA Cancer J Clin* (2005) 55(5):300–18. doi:10.3322/canjclin.55.5.300
 98. Teply BA, Hauke RJ. Chemotherapy options in castration-resistant prostate cancer. *Indian J Urol* (2016) 32(4):262. doi:10.4103/0970-1591.191239
 99. Aparicio AM, Harzstark AL, Corn PG, Wen S, Araujo JC, Tu SM, et al. Platinum-based chemotherapy for variant castrate-resistant prostate cancer. *Clin Cancer Res* (2013) 19(13):3621–30. doi:10.1158/1078-0432.CCR-12-3791
 100. Clegg NJ, Wongvipat J, Joseph JD, Tran C, Ouk S, Dilhas A, et al. ARN-509: a novel antiandrogen for prostate cancer treatment. *Cancer Res* (2012) 72(6):1494–503. doi:10.1158/0008-5472.CAN-11-3948
 101. Lovitt CJ, Shelper TB, Avery VM. Advanced cell culture techniques for cancer drug discovery. *Biology (Basel)* (2014) 3(2):345–67. doi:10.3390/biology3020345
 102. Sharma A. An ultraviolet-sterilization protocol for microtitre plates. *J Exp Microbiol Immunol* (2012) 16:144–7.
 103. Korff T, Augustin HG. Integration of endothelial cells in multicellular spheroids prevents apoptosis and induces differentiation. *J Cell Biol* (1998) 143(5):1341–52. doi:10.1083/jcb.143.5.1341
 104. Cox MC, Reese LM, Bickford LR, Verbridge SS. Toward the broad adoption of 3D tumor models in the cancer drug pipeline. *ACS Biomater Sci Eng* (2015) 1(10):877–94. doi:10.1021/acsbomaterials.5b00172
 105. Shelper TB, Lovitt CJ, Avery VM. Assessing drug efficacy in a miniaturized pancreatic cancer in vitro 3D cell culture model. *Assay Drug Dev Technol* (2016) 14(7):367–80. doi:10.1089/adt.2016.737
 106. Huber JM, Amann A, Koeck S, Lorenz E, Kelm JM, Obexer P, et al. Evaluation of assays for drug efficacy in a three-dimensional model of the lung. *J Cancer Res Clin Oncol* (2016) 142(9):1955–66. doi:10.1007/s00432-016-2198-0
 107. Breslin S, O'Driscoll L. The relevance of using 3D cell cultures, in addition to 2D monolayer cultures, when evaluating breast cancer drug sensitivity and resistance. *Oncotarget* (2016) 7(29):45745. doi:10.18632/oncotarget.9935
 108. Härmä V, Virtanen J, Mäkelä R, Happonen A, Mpindi JP, Knuutila M, et al. A comprehensive panel of three-dimensional models for studies of prostate cancer growth, invasion and drug responses. *PLoS One* (2010) 5(5):e10431. doi:10.1371/journal.pone.0010431
 109. Krausz E, de Hoogt R, Gustin E, Cornelissen F, Grand-Perret T, Janssen L, et al. Translation of a tumor microenvironment mimicking 3D tumor growth

- co-culture assay platform to high-content screening. *J Biomol Screen* (2013) 18(1):54–66. doi:10.1177/1087057112456874
110. Celli JP, Rizvi I, Blanden AR, Massodi I, Glidden MD, Pogue BW, et al. An imaging-based platform for high-content, quantitative evaluation of therapeutic response in 3D tumour models. *Sci Rep* (2014) 4:3751. doi:10.1038/srep03751
111. Sosa MS, Bragado P, Aguirre-Ghiso JA. Mechanisms of disseminated cancer cell dormancy: an awakening field. *Nat Rev Cancer* (2014) 14(9):611. doi:10.1038/nrc3793
112. Yeh AC, Ramaswamy S. Mechanisms of cancer cell dormancy – another hallmark of cancer? *Cancer Res* (2015) 75(23):5014–22. doi:10.1158/0008-5472.CAN-15-1370
113. Barbier M, Jaensch S, Cornelissen F, Vidic S, Gjerde K, de Hoogt R, et al. Ellipsoid segmentation model for analyzing light-attenuated 3D confocal image stacks of fluorescent multi-cellular spheroids. *PLoS One* (2016) 11(6):e0156942. doi:10.1371/journal.pone.0156942
114. Eder J, Sedrani R, Wiesmann C. The discovery of first-in-class drugs: origins and evolution. *Nat Rev Drug Discov* (2014) 13(8):577–87. doi:10.1038/nrd4336
115. Moffat JG, Rudolph J, Bailey D. Phenotypic screening in cancer drug discovery – past, present and future. *Nat Rev Drug Discov* (2014) 13(8):588–602. doi:10.1038/nrd4366
116. Swinney D. Phenotypic vs. target-based drug discovery for first-in-class medicines. *Clin Pharmacol Ther* (2013) 93(4):299–301. doi:10.1038/clpt.2012.236

Conflict of Interest Statement: The authors declare that the research was conducted in the absence of any commercial or financial relationships that could be construed as a potential conflict of interest.

Copyright © 2017 Mittler, Obeid, Rulina, Haguet, Gidrol and Balakirev. This is an open-access article distributed under the terms of the Creative Commons Attribution License (CC BY). The use, distribution or reproduction in other forums is permitted, provided the original author(s) or licensor are credited and that the original publication in this journal is cited, in accordance with accepted academic practice. No use, distribution or reproduction is permitted which does not comply with these terms.